Fundamentals and Applications of Metasurfaces

*Hui-Hsin Hsiao, Cheng Hung Chu, and Din Ping Tsai**

Metasurfaces have become a rapidly growing field of research in recent years due to their exceptional abilities in light manipulation and versatility in ultrathin optical applications. They also significantly benefit from their simplified fabrication process compared to metamaterials and are promising for integration with on-chip nanophotonic devices owing to their planar profiles. The recent progress in metasurfaces is reviewed and they are classified into six categories according to their underlying physics for realizing full 2π phase manipulation. Starting from multi-resonance and gap-plasmon metasurfaces that rely on the geometric effect of plasmonic nanoantennas, Pancharatnam–Berry-phase metasurfaces, on the other hand, use identical nanoantennas with varying rotation angles. The recent development of Huygens' metasurfaces and all-dielectric metasurfaces especially benefit from highly efficient transmission applications. An overview of state-of-the-art fabrication technologies is introduced, ranging from the commonly used processes such as electron beam and focused-ion-beam lithography to some emerging techniques, such as self-assembly and nanoimprint lithography. A variety of functional materials incorporated to reconfigurable or tunable metasurfaces is also presented. Finally, a few of the current intriguing metasurface-based applications are discussed, and opinions on future prospects are provided.

1. Introduction

Metamaterials (MMs) are three-dimensional (3D) artificial composite nanostructures with unprecedented properties for guiding and controlling the flow of electromagnetic waves, and have various intriguing novel optical effects and applications not achievable using natural materials.[1–4] However, it is still difficult to realize many of the proposed potential applications or devices, even after the enormous efforts in the past decade due to the challenges of fabricating complex 3D geometries and the inherent metallic losses of plasmonic elements at optical frequencies. Metasurfaces, characterized by a reduced dimensionality of MMs, have been gaining increasing attention as they possess great feasibility for realization and demonstrate exceptional abilities for light molding beyond that offered by conventional planar interfaces.[5] They usually consist of flat optical resonator arrays with spatially varying geometric parameters and subwavelength separation. Upon the interaction with light, engineering of the spatially varying optical response allows one to mold the optical wavefronts at will.

In contrast to conventional optical components that achieve wavefront engineering by phase accumulation through light propagation in the medium, metasurfaces give us new degrees of freedom to control the phase, amplitude, and polarization response with subwavelength resolution, as well as to accomplish wavefront shaping within a distance much less than the wavelength.[6] Their outstanding optical properties have led to the development of versatile ultrathin optical devices, whether showing novel optical phenomena or new functionalities outperforming their traditional counterparts. As the field of metasurfaces is rapidly growing, several review articles focusing on different areas can be found in the literature.[6–14] Here, we review the recent progress of metasurfaces from the fundamental theoretical background, physical realization, and fabrication, to their potential practical applications during the past few years.

2. Fundamental Theoretical Background – Generalized Snell's Law

Similar to the diffraction grating effect, the introduction of a metasurface induces a spatial distribution of phase discontinuities at the interface between two media. By applying Fermat's principle, as derived by Capasso's group,[5,15] or using the momentum conservation law for wavevectors in a diffraction grating system,[14] the reflection and refraction can be expressed by the following generalized formulas:

$$\begin{cases} k_{r,x} = k_{i,x} + \dfrac{\partial \phi}{\partial x} \\ k_{t,x} = k_{i,x} + \dfrac{\partial \phi}{\partial x} \end{cases} \quad (1)$$

where $k_{i,x}$, $k_{r,x}$, and $k_{t,x}$ are the x-components of the wavevectors of the incident, reflected, and transmitted light, respectively,

Dr. H.-H. Hsiao, Dr. C. H. Chu, Prof. D. P. Tsai
Research Center for Applied Sciences
Academia Sinica
Taipei 11529, Taiwan
E-mail: dptsai@phys.ntu.edu.tw
Dr. H.-H. Hsiao, Dr. C. H. Chu, Prof. D. P. Tsai
Department of Physics
National Taiwan University
Taipei 10617, Taiwan

DOI: 10.1002/smtd.201600064

and $\partial\phi/\partial x$ is the phase gradient. According to Equation (1), the reflected and transmitted waves can be redirected arbitrarily in their respective half space by engineering the spatial phase response of optical resonators at the interface (**Figure 1**). A primitive approach may simply use the dispersion of nanorod antennas for phase modulation. For example, the phase response of a transmitted (or reflected) beam at a fixed wavelength can be varied from 0 to π by changing the length of the nanorods.[5,16,17] However, to achieve a full control of wavefronts, a phase shift covering the range of 0 to 2π is required. Therefore, during the past few years, much effort has been invested in studying appropriate plasmonic or dielectric nanostructures that provide full phase manipulation and maintain large scattering efficiency. In the following section, we introduce the physical mechanisms, operation superiority, and limitations of several different types of metasurfaces (**Table 1**).

2.1. Multi-Resonance Metasurfaces

V-shaped antennas, consisting of two nanorods with equal length joined together at a certain angle, were the first proposed nanostructures that allow a phase variation of 0 to 2π. This plasmonic antenna supports two resonant modes, characterized as symmetric and antisymmetric modes according to their current distributions shown in **Figure 2**a.[5,18] The symmetric (antisymmetric) mode is excited when the polarization of incident electric field (E_{inc}) is parallel (perpendicular) to the symmetry axis of the antenna. When the incident wave is neither parallel nor perpendicular to the antenna symmetry axis, both resonant modes can be excited simultaneously. The hybridization of two eigenmodes results in two polarization states in scattered radiation:[19] one preserves the same polarization angle α as the incident light, and the other being $(2\beta - \alpha)$-polarized is attributed to anomalous components, where β is the angle between the antenna symmetry axis and the y coordinate, as indicated in Figure 2b. (The physics of the V-shaped antenna and its analytic model were discussed in detail in by Capasso and co-workers[19]) As initially demonstrated by Yu et al. in the mid-infrared[5] and later shown by Ni et al. in the near-infrared,[20] by properly choosing $\beta = 45°$ and $\alpha = 0°$ or 90°, the cross-polarized scattered light ($2\beta - \alpha = 90°$ or 0°) can have a large range of phases and amplitudes by varying the antenna geometry and orientations (Figure 2b). However, due to the coexistence of ordinary and anomalous reflection/refraction in this mechanism, the efficiency of the desired light-manipulation effect is quite low (Figure 2c). In addition, the fact that anomalous reflected/refracted optical beams possess different polarization with respect to incident light also limits its application.

Hui-Hsin Hsiao received her Ph.D. degree from the Graduate Institute of Photonics and Optoelectronics, National Taiwan University, in 2013. She is currently a postdoctoral Researcher at the Research Center for Applied Sciences, Academia Sinica and at the Department of Physics, National Taiwan University. Her current research interests include plasmonics, nonlinear plasmonics, and metasurfaces, along with their applications.

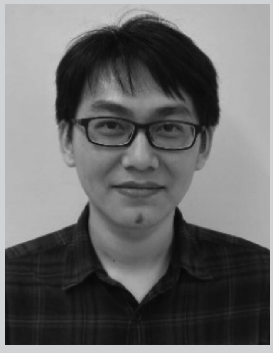

Cheng Hung Chu received his Ph.D degree in optoelectronic science from the National Taiwan Ocean University, Taiwan. He worked as an engineer at Taiwan Semiconductor Manufacturing Company (TSMC) in 2013–2014. He is currently a postdoctoral researcher of the Research Center for Applied Sciences, Academia Sinica. His current research interests are phase-change materials, laser fabrication, plasmonics, and optical data storage.

Din Ping Tsai received his Ph.D degree in physics from the University of Cincinnati, USA in 1990. He has been the Director and Distinguished Research Fellow of the Research Center for Applied Sciences, Academia Sinica since 2012. He is also the Distinguished Professor of the Department of Physics at the National Taiwan University. His current research interests are nanophotonics, near-field optics, plasmonics, metamaterials, biophotonics, and green photonics, along with their applications.

2.2. Gap-Plasmon Metasurfaces

The reflective-array metasurfaces, using the metal–insulator–metal structure as a basic building block, are constructed by adding a dielectric spacer and a metallic ground sheet beneath metallic antenna arrays. The optically thin dielectric layer allows strong near-field coupling between the top antenna array and their mirror dipoles in the metallic plane to achieve a 2π phase modulation. The induced currents on the nanoantennas and the ground plane are antiparallel, thus generating a strong magnetic field inside the insulator, known as gap–surface plasmon modes.[25,26] Figure 2d,e show the design of nanorod antennas[21] and H-shaped antennas[22] operating in the near-infrared and microwave regimes, respectively. The radiation phase can be efficiently tuned by simply changing the antenna length.[26–30] Meanwhile, since the reflected amplitude does

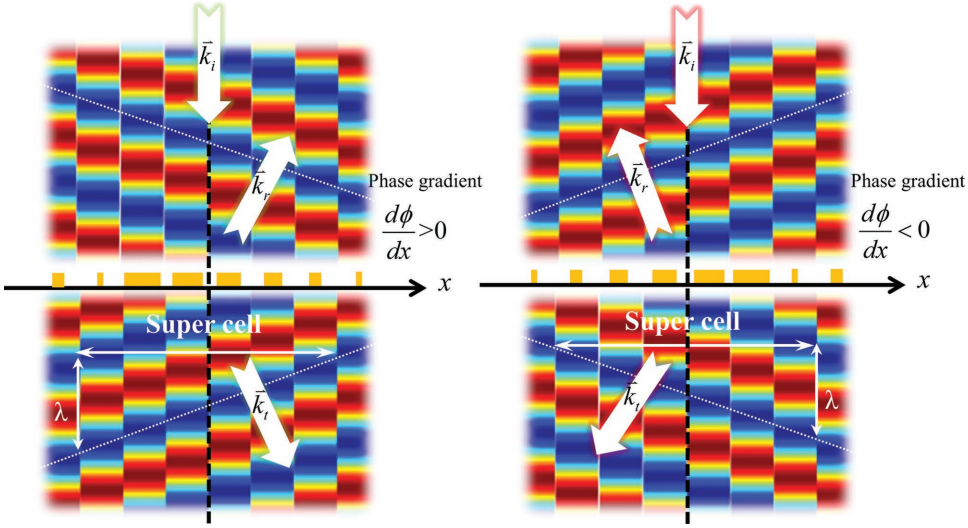

Figure 1. Metasurfaces composed of scatterers with spatial positive (left) and negative (right) phase-gradient response provide reverse-directed effective wavevectors along the interface, and thus the reflected and transmitted wavefront can be bent into arbitrary directions within their respective half space.

not vary too much from one unit structure to another, one can merely focus on phase response in the design stage. As transmission is suppressed by the metallic ground plane, the conversion efficiency to the anomalous reflection mode can reach as high as 80%.[21] In addition, this approach has the advantage that the reflected wave preserves the same polarization state with respect to the incident wave.

2.3. Pancharatnam–Berry-Phase Metasurfaces

Variations in phase or amplitude of the aforementioned metasurfaces are based on varying antennas geometry; another technique, known as Pancharatnam–Berry-phase (PB phase) metasurfaces, achieves a full phase control by adjusting the orientation angle of antennas with identical geometry.[31,32] Consider an anisotropic nanostructure under normal incidence, and t_o and t_e represent its complex transmission coefficients when the polarization of incoming light is along the two principle axes of the nanostructure, respectively. As the nanoresonator is rotated an angle θ from the x axis shown in Figure 2f, the transmission coefficients for this rotated system can be deduced via the operation of Jones matrix:[33,34]

$$\begin{aligned}\hat{t}(\theta) &= R(-\theta)\begin{pmatrix} t_0 & 0 \\ 0 & t_e \end{pmatrix}R(\theta) \\ &= \begin{bmatrix} \cos\theta & -\sin\theta \\ \sin\theta & \cos\theta \end{bmatrix}\begin{bmatrix} t_0 & 0 \\ 0 & t_e \end{bmatrix}\begin{bmatrix} \cos\theta & \sin\theta \\ -\sin\theta & \cos\theta \end{bmatrix} \\ &= \begin{bmatrix} t_0\cos^2\theta + t_e\sin^2\theta & (t_0 - t_e)\cos\theta\sin\theta \\ (t_0 - t_e)\cos\theta\sin\theta & t_0\sin^2\theta + t_e\cos^2\theta \end{bmatrix}\end{aligned} \quad (2)$$

where $R(\theta)$ is the rotation matrix. When the incident wave is circularly polarized (CP), the transmitted electric field ($E^t_{L/R}$) can be derived by applying matrix multiplication of Equation (2) and the Jones' vectors of left-handed CP (LCP) or right-handed CP (RCP) light $\hat{e}_{L/R} = (\hat{e}_x \pm i\hat{e}_y)/\sqrt{2}$ and written as:[35,36]

$$E^t_{L/R} = \hat{t}(\theta)\cdot\hat{e}_{L/R} = \frac{t_0 + t_e}{2}\hat{e}_{L/R} + \frac{t_0 - t_e}{2}e^{\pm i2\theta}\hat{e}_{R/L} \quad (3)$$

The first term in Equation (3) represents CP scattered waves with the same helicity as the incident wave, and the second term indicates that CP scattered waves with opposite helicity carry an additional Pancharatnam–Berry phase ($\pm i2\theta$). Therefore, a phase shift can be tuned from 0 to 2π for the opposite handedness radiation

Table 1. The unique properties of six categorized metasurfaces.

	Multi-resonance metasurfaces	Gap-plasmon metasurfaces	PB-phase metasurfaces	Huygens' metasurfaces	All-dielectric Huygens' metasurfaces/high-contrast metasurfaces
Outstanding Properties	• First proposed structures	• High efficiency • Co-polarized conversion	• Easy design • Broadband • Large fabrication tolerance	• High transmittance efficiency in the microwave and near-infrared regimes	• Low absorption loss at optical frequencies • High transmission efficiency
Limitations	• Low efficiency • Cross-polarized conversion	• Limited to reflective applications	• Limited to circularly polarized light operation	• Require multi-layered structures • Degrading performance in the optical regime	• Limited operation bandwidth in the visible • Limited choices of materials

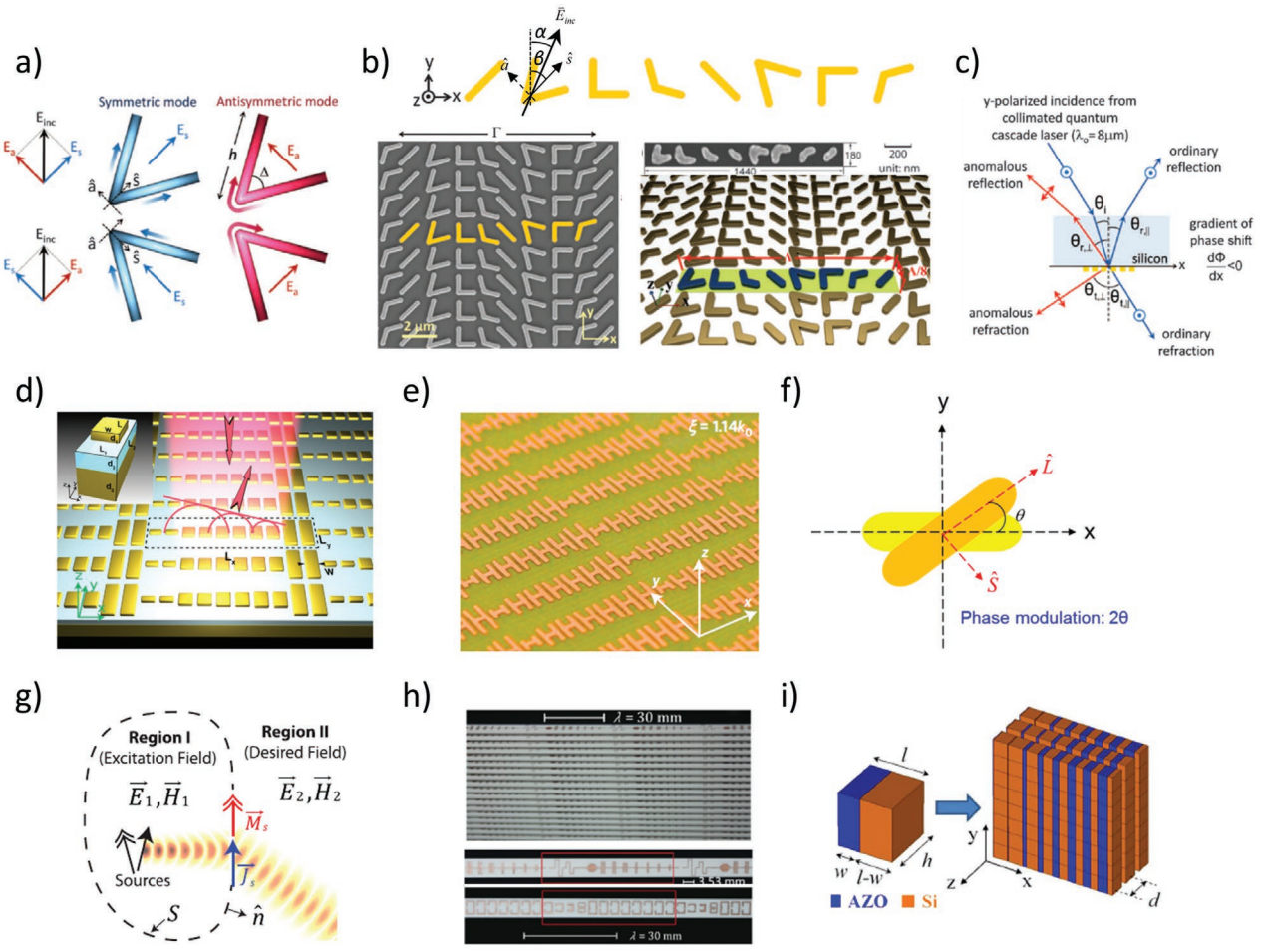

Figure 2. a) A V-shaped antenna supports two resonant modes characterized as symmetric and antisymmetric modes according to the current distributions. The symmetric and anti-symmetric modes are excited by components of the incident field along $\hat{s}$ and $\hat{a}$ axes, respectively. The schematic current distribution is represented by arrows indicating the direction of current flow and with brighter colors for larger currents. b) A supercell of V-shaped antennas with designed equal scattering amplitudes and constant phase gradient $\Delta\Phi = \pi/4$ between neighbors demonstrated at mid-infrared (left panel) and at near-infrared (right panel) regimes, respectively. c) Diagram of reflection and refraction of a V-shaped metasurface showing the coexistence of both co-polarized ordinary beams and cross-polarized anomalous beams. d) Schematic view of a near-infrared gap-plasmon metasurface. The left inset shows the basic building block made of a gold nanorod and a continuous gold film separated by a MgF_2 spacer. e) Photograph of a fabricated microwave gap-plasmon metasurface using H-shaped antennas with varying arm-lengths to manipulate the phase response. f) Schematic of a Pancharatnam–Berry-phase metasurface using nanorods as an example, where the phase response is solely determined by the orientation of nanorods θ relative to the x axis. g) Based on the surface equivalence principle, arbitrary field distributions in regions I and II can be achieved by properly design surface electric and magnetic currents that satisfy the boundary conditions. h) Upper panel: photograph of a fabricated microwave Huygens' metasurface consisting of a stack of identical circuit-board strips. Lower panel: copper traces on the top and bottom sides of the boards provide the necessary electric and magnetic polarization currents, respectively. i) Huygens' metasurface made of three stacked layers consisting of plasmonic (aluminum-doped zinc oxide) and dielectric (Si) materials as its basic building block (left). a–c) Reproduced with permission.[5] Copyright 2011, American Association for the Advancement of Science. b) Reproduced with permission.[20] Copyright 2012, American Association for the Advancement of Science. d) Reproduced with permission.[21] Copyright 2012, American Chemical Society. e) Reproduced with permission.[22] Copyright 2012, Nature Publishing Group. g–h) Reproduced with permission.[23] Copyright 2013, American Physical Society. i) Reproduced with permission.[24] Copyright 2013, American Physical Society.

as the nanoresonator is rotated from 0 to π.[37] Since this method uses oriented replicas of a single antenna design for phase modulation, it has the advantage of easy design, higher fabrication tolerance, and is beneficial to broadband applications.

2.4. Huygens' Metasurfaces

Since the insufficient coupling efficiency of single-layered plasmonic antennas to the phase-controlled mode significantly degrades the performance of transmitted-type metasurfaces, another approach based on the surface equivalence principle was proposed to minimize reflection by simultaneously tailoring the electric and magnetic polarizabilities at the interface. As shown in Figure 2g, to create desired field distributions in two regions with independent electromagnetic properties, surface electric and magnetic currents ($\vec{J}_s$ and $\vec{M}_s$) at the interface should satisfy the following relation for compensating the field discontinuities:[23]

$$\vec{J}_s = \hat{n} \times \left(\vec{H}_2 - \vec{H}_1\right), \quad \vec{M}_s = -\hat{n} \times \left(\vec{E}_2 - \vec{E}_1\right) \tag{4}$$

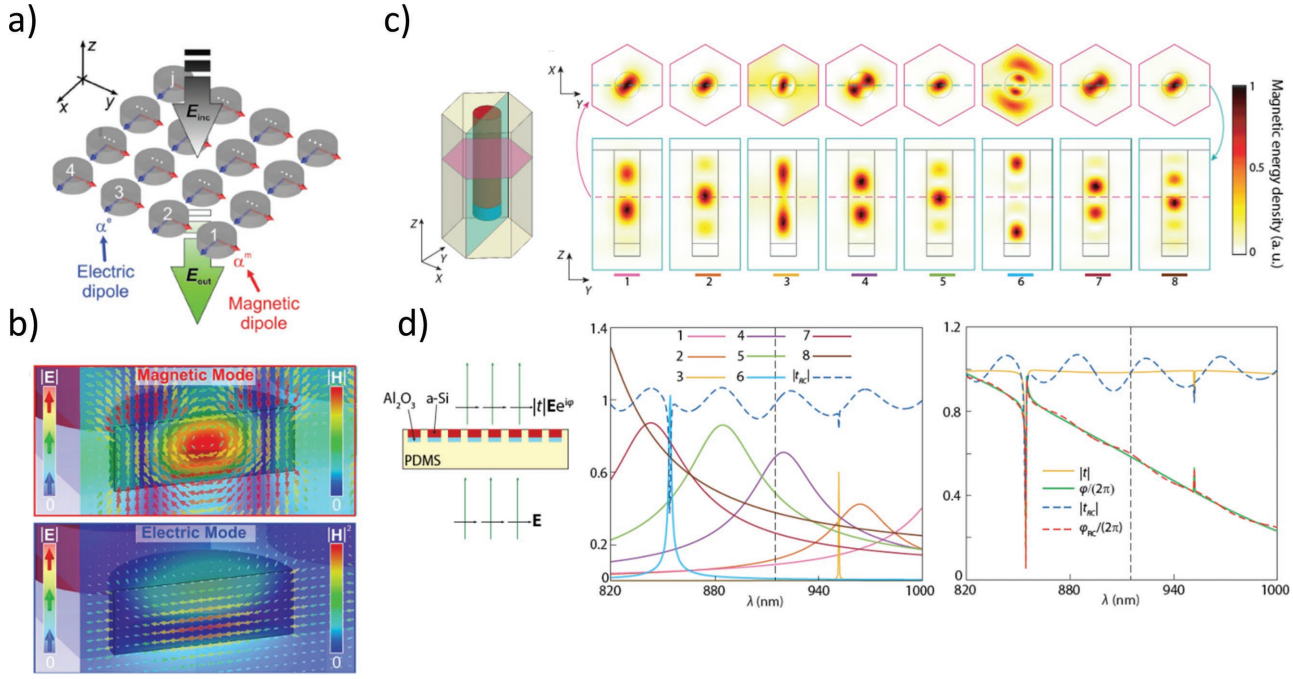

Figure 3. a) Schematic of dielectric Huygens' metasurface using arrays of nanodisks represented as electric and magnetic dipoles with polarizabilities α^e and α^m under *x*-polarized illumination. b) Electric (colored arrows) and magnetic (plain color) field distributions for the magnetic (top) and electric (bottom) mode of periodic Si nanodisks. c) Magnetic-energy-density distributions of 8 dominant resonant modes of a nanopost array viewing from the horizontal (top) and vertical (bottom) cut planes of the unit cell shown in the left panel. d) Left panel: diagram of the simulation setup for calculating transmission coefficients of nanopost arrays under normal incidence. Middle panel: the reconstructed transmission amplitude from 8 dominant resonant modes. Right panel: a comparison between the calculated transmission amplitude and phase of periodic nanoposts and reconstructed transmission amplitude and phase using the 8 dominant resonant modes. $|t_{RC}|$: reconstructed transmission amplitude, ϕ_{RC}: reconstructed transmission phase. a,b) Reproduced with permission.[40] Copyright 2015, Wiley-VCH. c,d) Reproduced with permission.[47] Copyright 2016, Nature Publishing Group.

With an arbitrary form of the impinging and desired waves, the design of Huygens' metasurfaces may comprise nonperiodic or multilayered structures in order to engineer surface impedances locally. For example, Pfeiffer and Grbic used a supercell consisting of 12 patterned elements to realize a beam deflector with 86% transmittance in the microwave regime (Figure 2h).[23] Monticone et al. proposed a stack of three-layered metasurfaces, constructed from a combination of dielectric and plasmonic nanoblocks functionalized as nanocapacitors and nanoinductors, respectively, for light bending in the near-infrared range with a theoretical efficiency of 75% (Figure 2i).[24] However, the performance of Huygens' metasurfaces is much poorer at optical frequencies with the demonstrated efficiency remaining below 20%.[38] This is due to the weak magnetic response of natural materials and intrinsic metallic loss of plasmonic elements in the visible regime.

2.5. All-Dielectric Huygens' Metasurfaces

As plasmonic metasurfaces suffer from increasing dissipative losses at optical frequencies, as well as several undesirable loss channels occurring during the phase-modulation process, such as diffraction, ordinary reflection/refraction, and polarization conversion losses, this initiates a new branch of research working with the dielectric analogs of metasurfaces. The high-refractive-index dielectric nanoparticles or nanodisks were found to be able to generate spectrally overlapping electric and magnetic resonances with comparable strengths, which is critical for the achievement of an optimal transmitted efficiency with the Huygens' metasurfaces.[39–41] Different from their metallic counterparts where the high metallic losses at visible frequencies cause vanishing fields inside nanoparticles and thus lead to a negligible magnetic response, dielectric nanoparticles with their low intrinsic losses are able to couple the incoming wave to generate circular displacement currents inside the nanostructures and give rise to a strong magnetic dipole resonance (**Figure 3**a,b).[42–45] For example, Kivshar's group utilized arrays of high-permittivity silicon (Si) nanodisks to experimentally demonstrate a 0-to-2π phase coverage with transmission efficiency more than 55% in the near-infrared regime.[40] A beam deflector based on all-dielectric Huygens' metasurfaces was also demonstrated, with measured efficiency as high as 45% at visible frequencies.[46]

2.6. High-Contrast Metasurfaces

High-contrast metasurfaces, composed of disconnected high-refractive-index dielectric scatterers positioning into the periodic 2D lattice, are also capable of achieving simultaneous phase and polarization control with high transmission (Figure 3c).[48] Each nanoscatterer can be treated as an individual truncated waveguide, which supports multiple Fabry–Perot resonances with low quality factors.[49] Different from all-dielectric Huygens' metasurfaces with dominant electric and

magnetic dipole resonances, the resonant modes of high-contrast metasurfaces contain electric and magnetic dipoles, quadrupoles, and higher-order multiples (Figure 3d).[47] Owing to the large refractive-index difference between the nanoscatterers and their surroundings, optical energy is strongly concentrated inside each nanoscatterer so that transmittance property is primarily determined by the nanoscatterer geometry, while the optical coupling among them has negligible effect. High-contrast metasurfaces have been demonstrated as a polarization beam splitter with measured transmission efficiency larger than 70% for both *x*- and *y*-polarized light.[48]

3. Fabrication

Photolithography, electron-beam lithography, and focused-ion-beam lithography are the conventional surface-lithography technologies for patterning nanostructures. For the fabrication of metasurfaces, the choice of fabrication technique should consider the inherent advantages and disadvantages of these technologies that satisfying the process requirements, such as resolution, throughput, reliability, reproducibility, and cost efficiency. Photolithography is the most widely used fabrication technology in semiconductor integrated circuits with high throughput at the micro- and nanoscale (**Figure 4**a). The patterns are transferred from photomasks to photoresists after the exposure and development steps. After the etching, depositing, and lift-off process, nanostructures are formed on the substrates. Electron-beam lithography is a maskless system capable of directly drawing arbitrary patterns with several nanoscale featured sizes (Figure 4a). In addition, the focused-ion-beam technique is also a straightforward versatile nanofabrication method by removing and depositing the materials in one step (Figure 4b).

In order to meet the growing demands of nanofabrication, many promising fabrication techniques have been developed and incorporated into the fabrication of metasurfaces, such as interference lithography,[50,54] self-assembly,[51] and nanoimprint lithography.[52] Interference lithography is a different modality of photolithography, whose pattern shapes are based on the interference of two or more coherent laser beams. For example, the periodic grating structures can be fabricated by two-beam interference lithography with two plane waves. More complex periodic 2D or 3D structures, on the other hand, can also be produced by advanced interference lithography, such as multiple-exposure and non-coplanar beams (Figure 4c). Self-assembly lithography is an efficient and facile method with which to pattern various large-area nanostructures, including

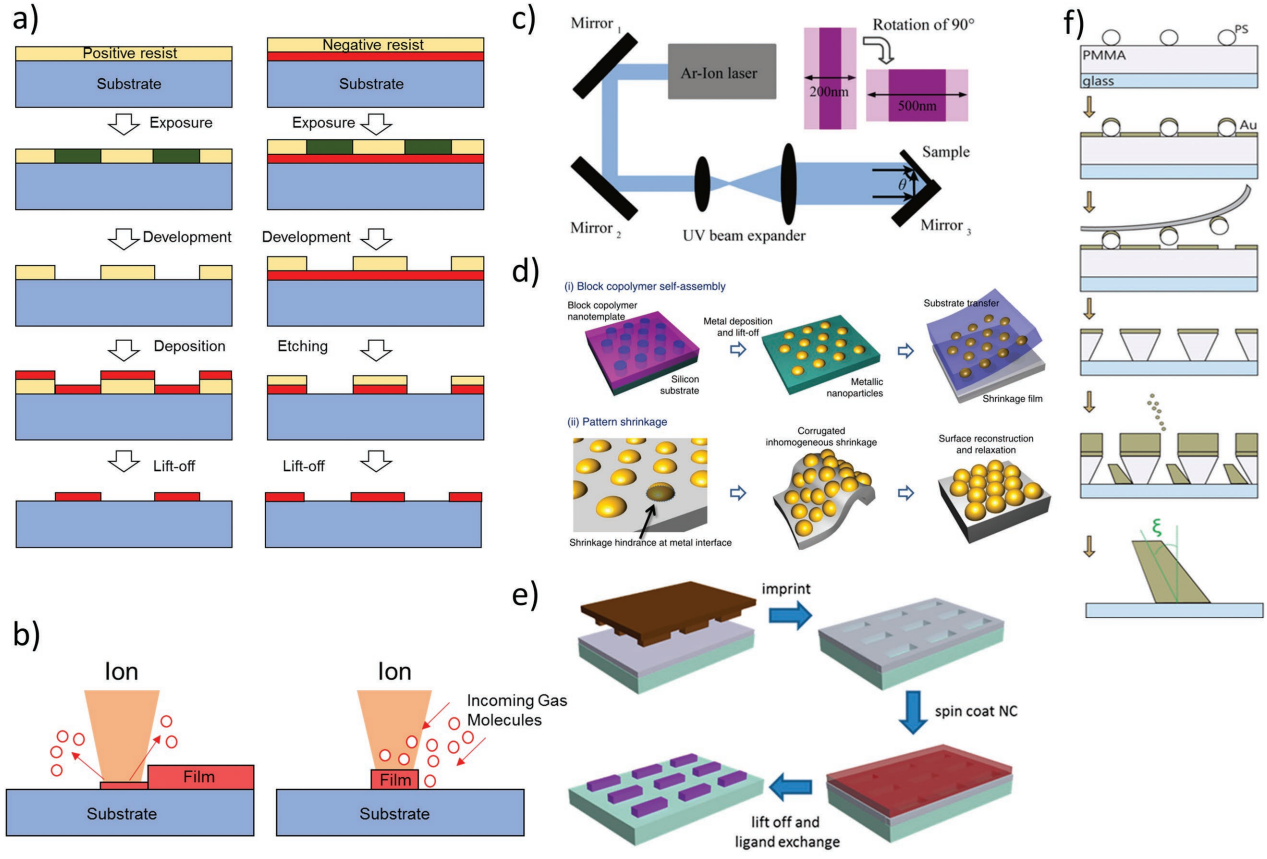

Figure 4. a) Photolithography/e-beam lithography process. b) Focused-ion beam. c) Interference lithography. d) Self-assembly. e) Nanoimprint lithography. f) Hole-mask colloidal lithography and off-normal deposition. c) Reproduced with permission.[50] Copyright 2015, American Institute of Physics. d) Reproduced with permission.[51] Copyright 2015, Nature Publishing Group. e) Reproduced with permission.[52] Copyright 2015, American Chemical Society. f) Reproduced with permission.[53] Copyright 2016, American Chemical Society.

Table 2. Tuning mechanisms for metasurfaces.

Mechanism	Deformation	Phase states	Optical anisotropic	Distribution	Carrier concentration
Functional materials	• PDMS • PMMA	• VO_2 • GST	• Liquid crystals	• Microfluidic	• InSb • ITO

chains, sheets, and 3D constructions, where the system is spontaneously assembled by intermolecular balance of attractive and repulsive forces (Figure 4d). Nanoimprint lithography is a low-cost, large-area, and high-throughput alternative technique for replication of subwavelength ordered structures in a single patterning step. The hard mold with nanoscale surface-relief features is pressed onto a substrate coated with a moldable polymeric resist to replicate the patterns via mechanical deformation (Figure 4e).

In addition, several hybrid patterning processes have been developed for the realization of more complex nanostructures. For example, hole–mask colloidal lithography and off-normal deposition are combined to fabricate directional metasurfaces with tilted nanopillars.[53] Hole-mask colloidal lithography using roller template stripping has been proposed to pattern subwavelength metallic nanoholes, nanodisks, wires, and pyramids by taking advantage of plastic materials with the flexible and stretchable property.[55] First, the metal film is deposited on a poly(methyl methacrylate) (PMMA) substrate with polystyrene nanospheres, and then the nanospheres are removed by tape stripping to form the hole-mask. Next, by deposition of the metal with a tilted angle and removal of the PMMA, the tilted nanopillars are produced (Figure 4f).

Recently, a variety of functional materials have been applied to studies of tunable metasurfaces (**Table 2**). For example, flexible substrates made of poly(dimethylsiloxane) (PDMS) are used for conformal metasurfaces[47] and mechanically reconfigurable metasurfaces.[56] The high flexibility and stretchability of PDMS makes it possible for the surfaces to be wrapped and for them to experience an external pulling force. Liquid crystals with broadband optical nonlinearity and birefringence are the most commonly used materials for the dynamic control of the optical properties. The refractive-index change of a liquid crystal can be externally tuned by temperature, light, and electric or magnetic fields.[57,58] Phase-change materials have also been extensively utilized in optical data-storage systems and nanophotonic systems based on their tunable optical properties. For example, vanadium dioxide (VO_2)[59–61] and GeSbTe alloys [62] exhibit dramatic difference in optical properties between various phase states. Their reversible phase transition can be triggered by thermal energy. In addition, 2D materials with special optical and electrical properties are integrated to electrically tunable metasurfaces, where the charge-carrier density can be controlled by the gate voltage to stimulate a change in the optical properties.[63] Microfluidic technology can also be applied to tunable metalenses by controlling the air pressure of the pneumatic valves to change the distribution of liquid metals within each unit cell.[64]

4. Applications

The recent advances in metasurfaces have been applied to the demonstrations of many exotic optical phenomena and various useful planar optical devices. Many of these metasurface-based applications are promising alternatives to replace conventional optical devices, as they largely benefit from ultrathin, lightweight, and ultracompact properties, provide the possibility of overcoming several limitations suffered by their traditional counterparts, and demonstrate versatile novel functionality.[65] In the following section, the recent progress of metasurface-based applications aimed at polarization control and wavefront manipulation is discussed (**Figure 5**).

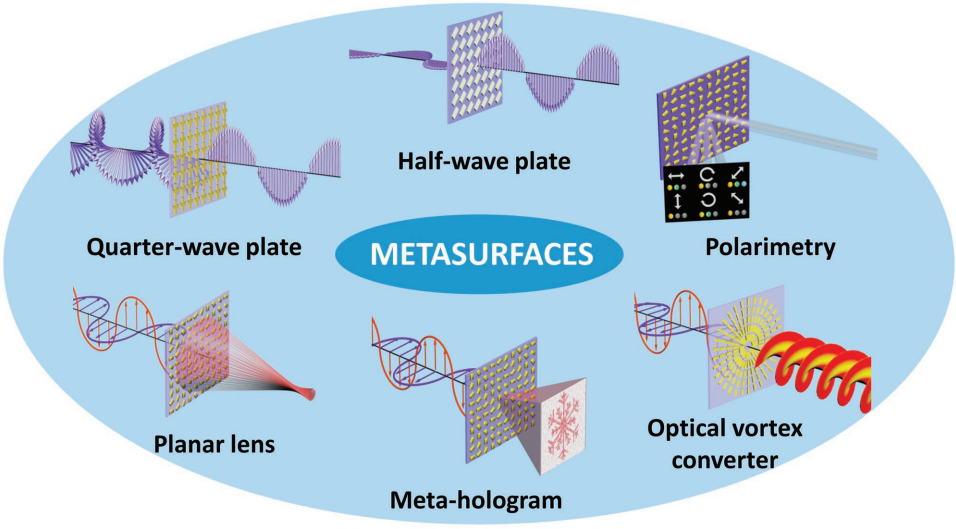

Figure 5. Metasurface-based applications on polarization control and wavefront shaping.

4.1. Polarization Manipulation and Detection

4.1.1. Quarter-Wave Plates

Conventionally, the polarization state of light can be modulated by the birefringence of crystals, where the required phase retardation between two orthogonally polarized wave components is accumulated through light propagation. As a result, the polarization control setups are usually bulky and suffer from several limitations such as narrow operating bandwidth and limited choice of materials. This boosts the development of metasurface-based wave plates operating in different frequency regimes. **Figure 6** shows several examples of quarter-wave plates (QWPs) based on the ultrathin metasurface design.[19,61,66–71] The manipulation of the polarization state of electromagnetic waves can be realized by splitting the incident light into two orthogonal components and controlling the required phase delay between them. For example, Yu et al. fabricated a broadband and background-free QWP, where high-quality CP light with ellipticity > 0.97 can be generated over a broad wavelength range (λ = 5 to 12 μm) as shown in Figure 6a.[19] Using the V-shaped antennas discussed above, they designed two subunits with different antenna orientations so that the corresponding $(2\beta - \alpha)$-polarized scattered light in each subunit satisfies the relation of $(2\beta_1 - \alpha) - (2\beta_2 - \alpha) = 90°$, which leads to the splitting of incident radiation into two orthogonal states. The spatial phase gradient allows the scattered light to be bent away from the propagation direction of the incident beam and results in a background-free output beam. The required phase delay between these orthogonal components was controlled by the offset distance between the subunits.

The anisotropic optical response of asymmetrically shaped nanoantennas can also be applied to the realization of ultrathin metasurface-based QWPs. For example, Zhao and Alù[67] and Chen et al.[52] utilized the detuned plasmonic resonances of two orthogonal nanorods with different sizes to perform circular-to-linear (CTL) polarization conversion in the visible and the near-to-mid-infrared regimes, respectively. Upon the illumination of horizontally and vertically linearly polarized (LP) light, two pronounced resonant dips can be found, corresponding to the dipolar resonances of *x*-oriented and *y*-oriented nanorods, respectively. By operating in the off-resonant regime between the resonances, the transmission coefficient between the *x*- and *y*-polarized light exhibited a phase difference ($\Delta\Phi = \Phi_{xx} - \Phi_{yy}$) close to 90° accompanied by a wavelength-dependent transmission amplitude ratio (T_{yy}/T_{xx}) (Figure 6b). Therefore, such devices can convert CP input light into transmitted LP light with a measured degree of linear polarization larger than 80% and with a wavelength-dependent polarization angle. To accomplish the reverse, operating as linear-to-circular (LTC)

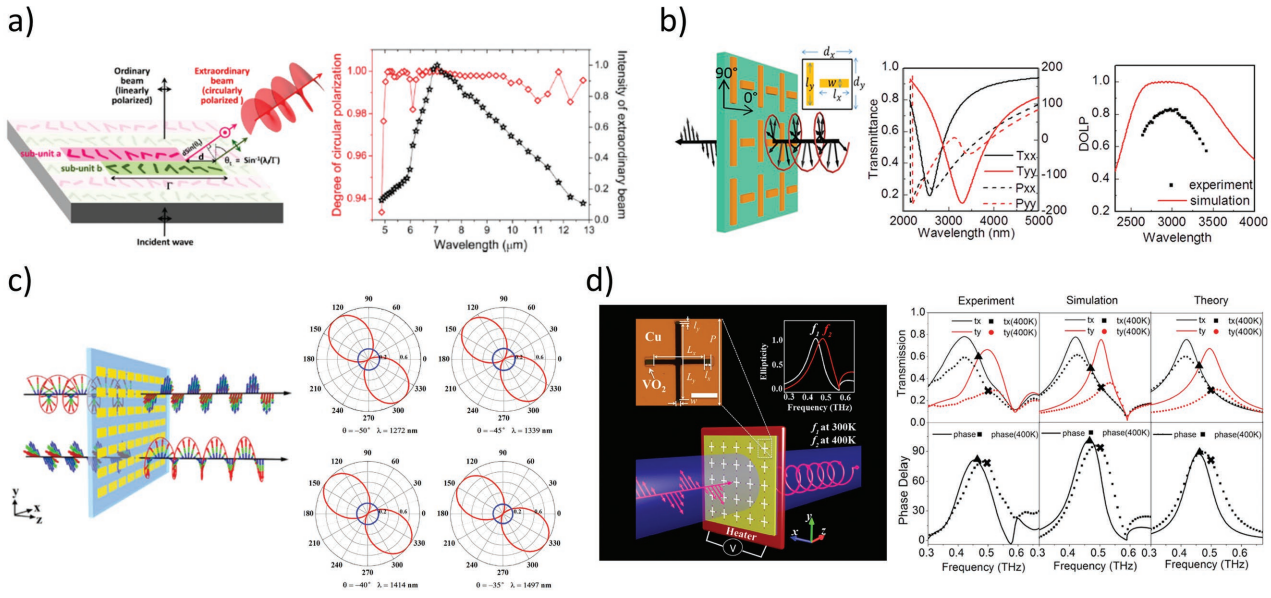

Figure 6. a) Left panel: diagram of a background-free metasurface-based QWP consisting of two V-shaped antenna subunits that generate two co-propagating waves with orthogonal linear polarizations, equal amplitudes, and a $\pi/2$ phase difference upon LP incidence. Right panel: full wave simulations of degree of circular polarization and the extraordinary beam intensity. b) Left panel: schematic view of a CTL polarization converter with inset showing a unit cell consisting of two nanorods forming a T-shaped pattern. Middle panel: the calculated transmittance (solid curve) and phase (dashed curve) spectra under *x*- and *y*-polarized excitations. Right panel: the measured (black dots) and calculated (red curve) degree of linear polarization for CP input light as a function of wavelength. c) Left panel: sketch of CTL and LTC polarization converters using nanorod arrays. Right panel: theoretical calculations of the polarization angle of LP input light (red curves) at each sampling wavelength that gives rise to converted CP output light (blue curves). d) Left panel: a switchable THz QWP made of arrays of cross-shaped apertures that covert linear 45°-polarized light to CP light, and the operating frequency can be switched via the VO_2 phase transition controlled by a resistive heater. Right panel: the transmission (upper) and phase difference (lower) for *x*- and *y*-polarized incidence at 300 K (solid curves) and 400K (dot curves) obtained through the experimental measurements, numerical simulations, and theoretical calculations. a) Reproduced with permission.[19] Copyright 2012, American Chemical Society. b) Reproduced with permission.[52] Copyright 2015, American Chemical Society. c) Reproduced with permission.[70] Copyright 2014, Nature Publishing Group. d) Reproduced with permission.[61] Copyright 2015, Nature Publishing Group.

polarization conversion, the polarization angle of the incident LP light should be carefully tuned at each wavelength so that the transmitted components have equal amplitudes along the principle axes of the sample, owing to the dispersion of the amplitude ratio. Instead of using two orthogonally patterned nanorods, Li et al. theoretically demonstrated CTL and LTC polarization conversion by exploiting the orthogonal optical resonant modes of a single nanorod (Figure 6c).[70] The simulated transmittance for CTL polarization conversion reaches more than 40% in the wavelength range of 1100 nm to 2000 nm. With careful manipulation of the incident electric-field polarization angle at each sampling wavelength, transmittance for LTC polarization conversion can be achieved over 30% in the range of 1170 nm to 1590 nm.

Wang et al. further fabricated a switchable terahertz (THz) QWP by inserting VO_2 into arrays of asymmetrically cross-shaped apertures (Figure 6d).[61] The lengths of the orthogonal slots were designed to possess a phase shift of 90° under the excitation of orthogonal LP light.[71] By manipulating the phase transition of VO_2 at different temperatures via a resistive heater, the effective length of the resonators can be altered and thus the operating frequency of the QWP can be switched.

4.1.2. Half-Wave Plates

Another category of polarization conversion metasurfaces works as half-wave plates (HWPs), rotating the direction of linear polarization.[26,33,69,72–77] An example is shown in **Figure 7**a, which is composed of an array of 45°-rotated brick-shaped nano-antennas, a dielectric spacer, and a continuous metallic film. Under *x*-polarized light illumination, E_i can be decomposed into two perpendicular components (E_{ui} and E_{vi}) and excited orthogonal electric dipoles along the two principle axes of the nanobricks, respectively. When the reflected coefficients of detuned long and short-axis resonances reach equal amplitudes with a phase difference of π, *x*-polarized incident light can be transformed to *y*-polarized light in reflection.[72] Based on this principle, Grady et al. demonstrated an HWP with measured cross-polarized reflection as high as 80% between 0.73 to 1.8 THz.[73] Such highly efficient performance is attributed to the constructive interference of the partially cross-polarized reflected fields within the Fabry–Perot-like cavity, and can be sustainable over a wide range of incident angles. Ding et al. further demonstrated a background-free HWP in the near-infrared range by designing a supercell with a spatial phase gradient of 0 to 2π for the cross-polarized reflected waves (Figure 7a).[72]

Metasurface-based HWPs can also be operated in transmission mode. As demonstrated by Grady et al., two orthogonal metallic gratings were introduced on the top and bottom of an 45°-rotated nanobrick array as shown in Figure 7b.[73] The back grating allows the transmission of a cross-polarized light beam while blocking the co-polarized light beam. The front grating reflects cross-polarized light without blocking incident light and co-polarized components. The multi-reflection process continues within this composite structure, resulting in a constructive interference that shows cross-polarized transmission over 50% from 0.52 to 1.82 THz.

Jiang et al. utilized arrays of strongly coupled nanorods with tailored aspect ratio to construct a reflective HWP (Figure 7c).[69] The measured polarization conversion ratio and reflectance were higher than 92% from the visible to near-infrared with a wide field of view (FOV) up to ±40°.

Fan et al. demonstrated a freely tunable polarization rotator by using a trilayer metasurface with three rotatable metallic gratings (Figure 7d).[74] The polarization angle of the input LP light can be altered freely due to the multi-wave interference in this tri-grating structure. With the optimal geometry design, such as the thicknesses, the periods, and the separation distances of three gratings, constructive interference of multiple transverse-magnetic waves can be achieved, eventually leading to a nearly perfect polarization conversion. The measured cross-polarized transmittance reaches 90% within a broad bandwidth (Figure 7d). In addition to the 90° polarization conversion as HWPs, the polarization rotation angle can be freely tuned from the range of –90° to 90° by simply rotating the three composite grating layers. As the rotation angle decreases, the working bandwidth increases while the conversion efficiency slightly decreases (Figure 7d).

Shaltout and co-workers applied PB phase metasurfaces to rotate LP light by 45° at near-infrared frequencies (Figure 7e).[75,76] For an antenna array with orientation angles varying from 0 to π, the incident CP light acquires an additional PB phase term from 0 to 2π (-2π) when converted to its opposite helicity. According to Equation (3), since the converted LCP and RCP light beams acquire an opposite PB phase, they will be scattered to opposite directions (**Figure 8**a).[36] Such spatial separation for different CP states is known as the photonic spin Hall effect (PSHE).[75,78] As LP light can be regarded as the superposition of LCP and RCP components, a metasurface consisting of two subunits of antenna arrays rotating in the opposite directions can generate converted LCP light from one subunit directed in parallel to converted RCP light from the other, upon LP light illumination. (Figure 7e). These two CP waves can be utilized to effectively retrieve an LP output beam with its polarization angle depending on the spatial offset between the subunits. Wu et al. employed a reflective aluminum (Al) metasurface composed of six types of supercells with different offsets to simultaneously generate six polarization light beams (two CPs and four LPs) upon one LP illumination (Figure 7f).[77]

4.1.3. Polarimetry

The control of metasurfaces over polarization motivates the implementation of polarimetry devices for sensing the polarization state or determination of the Stokes parameters of an arbitrary light source. For example, Shaltout et al.[75] and Wen et al.[36] utilized the PSHE to demonstrate polarization sensing and spectroscopy devices that perform spatial separation of LCP and RCP light in reflected-type and transmitted-type PB phase metasurfaces, respectively (Figure 8a,b). The scattering intensity ratio of two CP states can be used as an indicator to determine the ellipticity and helicity of incident light (Figure 8c).[36]

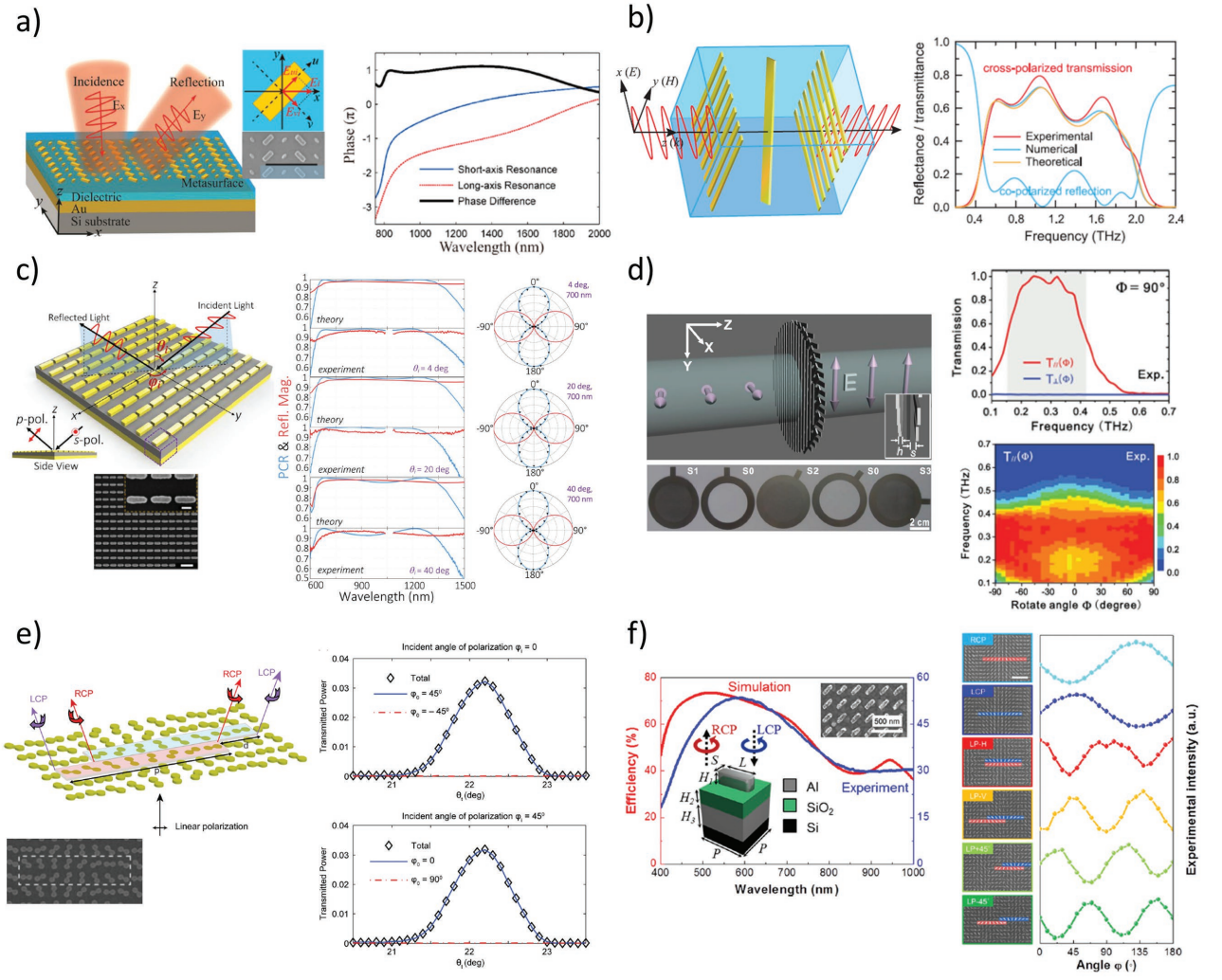

Figure 7. a) Left panel: geometry of a reflective background-free HWP. Insets: the coordinate geometry of the basic building block and SEM image of part of fabricated metasurface with light blue color indicated the supercell. Right panel: the reflected phase spectra for incident light polarized along the *u* and *v* axes, respectively, and the corresponding phase difference between them. b) Left panel: sketch of a unit cell for transmitted HWP. Right panel: cross-polarized transmittance obtained through experimental measurements, numerical simulations, and analytical calculations. c) Left panel: diagram of metasurface-based HWPs utilizing the strong near-field coupling of nanorod antennas to achieve polarization rotation with wide FOV. The inset shows an SEM image of the fabricated sample. Middle panel: the calculated and measured polarization conversion ratio (blue curves) and reflection (red curves) spectra at different oblique angles of incidence. Right panel: the calculated and measured polarization states of incident and reflective waves at 700 nm for three oblique incident angles of 4°, 20°, 40°. d) Left panel: schematic of a freely tunable THz polarization rotator consisting of three-grating-layer structure with its inset showing part of the lateral view. The lower part shows a photograph of the five components of the polarization rotator. Right panel: measured transmission spectra for components polarized parallel ($T_{\parallel}(\Phi)$) and perpendicular ($T_{\perp}(\Phi)$) to the desired polarization state when Φ is designed to be 90° (upper). The measured $T_{\parallel}(\Phi)$ when Φ is varied from −90° to +90° (lower). e) Left panel: schematic view of polarization-controlled metasurface using two PB-phase subarrays (blue and red) rotating in opposite directions. The inset shows an SEM image of the fabricated sample with the supercell highlighted by the dashed rectangle. Right panel: experimental results show the rotation of LP light by 45°. f) Left panel: the calculated and measured conversion efficiency of reflective Al metasurfaces with inset showing an SEM image of the fabricated sample. Right panel: measured scattering intensity of six polarizations. The inset displays the corresponding SEM images of the fabricated samples with each supercell highlighted by colors. a) Reproduced with permission.[72] Copyright 2015, American Chemical Society. b) Reproduced with permission.[73] Copyright 2013, American Association for the Advancement of Science. c) Reproduced with permission.[69] Copyright 2014, Nature Publishing Group. d) Reproduced with permission.[74] Copyright 2015, Wiley-VCH. e) Reproduced with permission.[76] Copyright 2014, American Chemical Society. e) Reproduced with permission.[77] Copyright 2017, American Chemical Society.

Pors et al. used a composite plasmonic metagratings for simultaneous determination of Stokes' parameters of an incident beam.[79] As the determination of the light polarization state requires the respective intensities in three orthonormal polarization bases of (0°, 90°), (45°, −45°) and (LCP, RCP),[80] three set of nanobrick supercells were integrated into the designed metasurface via an interweaving arrangement (Figure 8d). The incident optical beam can thus interact with three bases simultaneously and split to the associated two orthogonal states upon illumination once.

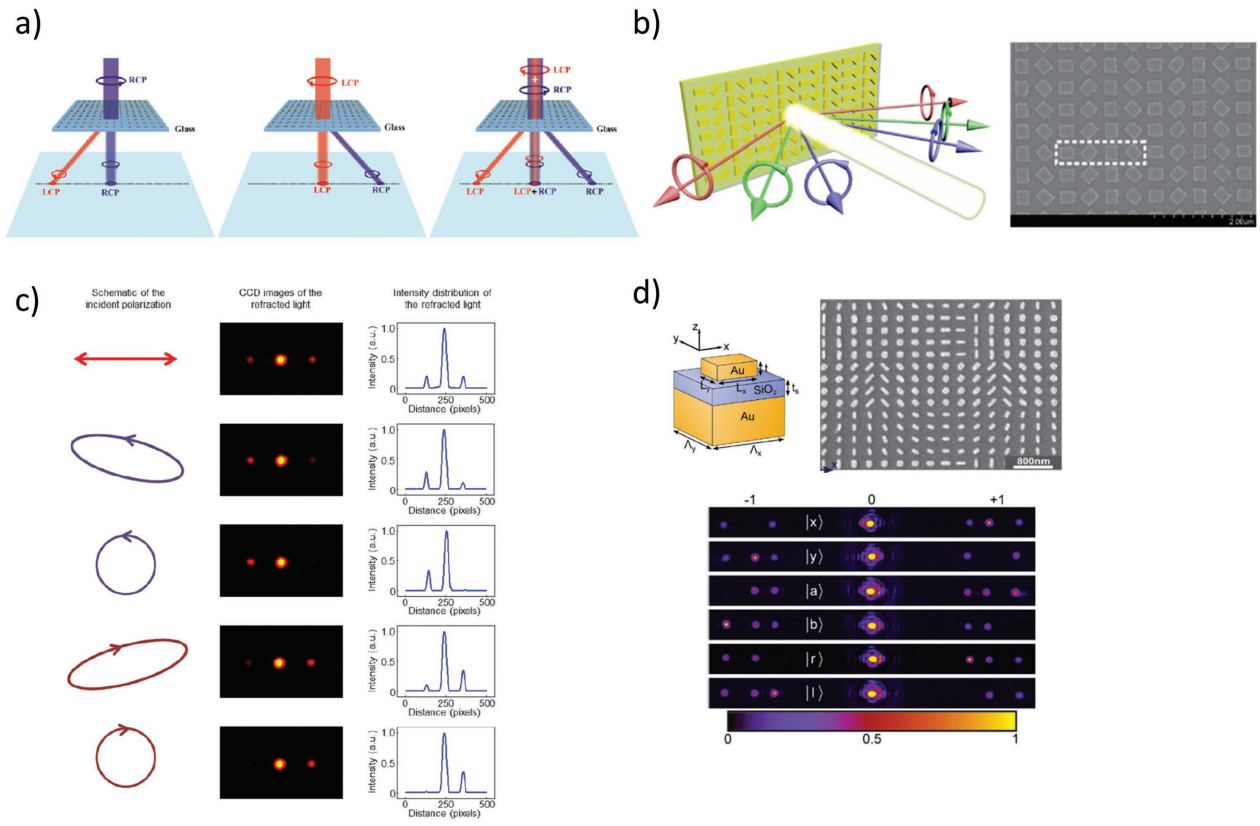

Figure 8. a) Schematic illustration of PSHE. The transmitted CP light with the same helicity as the incident wave propagates along the regular direction, while the converted CP light with the opposite helicity acquires an additional PB phase term and thus is refracted to anomalous directions. As a linearly or elliptically polarized incident wave can be considered as the superposition of LCP and RCP components, the converted RCP and LCP light acquires an opposite additional PB phase term and is scattered to opposite directions. b) Left panel: PSHE demonstrated by reflective PB-phase metasurfaces. Right panel: SEM image of a fabricated sample. c) CCD images of the refracted light spots under different polarization states of incidence. d) Upper panel: SEM image of a metagrating that enables simultaneous determination of Stokes' parameters with left inset showing its basic building block. Lower panel: experimental optical images of the diffraction spots corresponding to the six polarization components for the determination of Stokes' parameters. a) Reproduced with permission.[36] Copyright 2015, Optical Society of America. b) Reproduced with permission.[75] Copyright 2015, Optical Society of America. c) Reproduced with permission.[36] Copyright 2015, Optical Society of America. d) Reproduced with permission.[79] Copyright 2015, Optical Society of America.

4.2. Wavefront Shaping

4.2.1. Planar Metalenses

The wavefront engineering for conventional refractive lenses is based on the surface topography or the spatial refractive-index variation of the optical transparent media. Under such a framework, the beam profiles are altered according to the phase accumulation along the optical path through these lensing devices. To achieve the phase profile equivalent to conventional lenses, metasurfaces should impose the following phase profile to convert incident planar wavefronts into spherical ones:[81,82]

$$\varphi(x,y) = -\frac{2\pi}{\lambda}\left(\sqrt{x^2+y^2+f^2}-f\right) \quad (5)$$

where λ is the wavelength in free space, and f is the focal length of the lens. Planar metasurface lenses, so-called metalenses, have been experimentally demonstrated using V-shaped antennas at telecom wavelengths.[82] However, the efficiency of these metalenses is relatively low due to the weak light coupling to the single-layered plasmonic antennas and focusing only the cross-polarized scattering component. The complementary V-shaped apertures were also applied to fabricate flat lenses in the visible.[83] In addition, nanorods[34,84] and U-shaped apertures[35] have been used to create planar lenses based on the PB-phase technique, where the required phase profile is introduced when CP incident light is converted to its opposite helicity. Recently, Capasso's group demonstrated diffraction-limited metalenses with efficiency as high as 86% by using high-aspect-ratio titanium dioxide (TiO_2) nanofins with PB phase rotational morphology (**Figure 9**a).[85] The focal spots at their design wavelengths are smaller by a factor of ≈1.5 than those from a commercial lens. The TiO_2 building blocks were further used to construct two interlaced arrays that focus incident light beams with opposite helicities into two distinct foci, demonstrating a chirality-distinguishable imaging system.[86]

As conventional lenses suffer from severe chromatic aberrations due to the dispersion of the phase accumulated by light during propagation, many metasurface-designed lenses

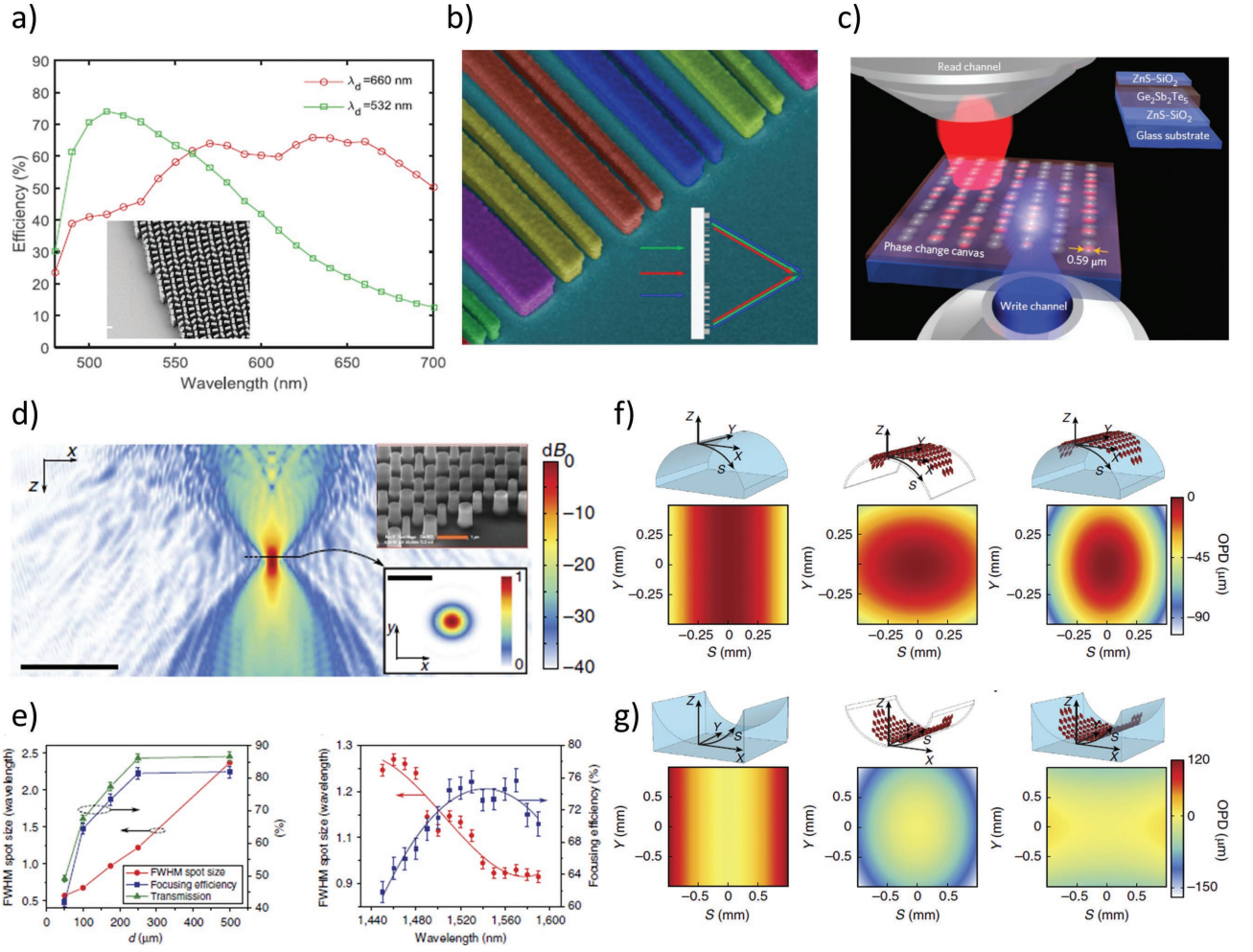

Figure 9. a) Measured focusing efficiency of a metalens consisting of high-aspect ratio TiO_2 with PB-phase rotational morphology. The inset shows an SEM image of part of a fabricated sample. b) False-colored side-view SEM image of a telecom achromatic metalens using two rectangular a-Si resonators separated by a gap as the basic building block. c) Schematic of reconfigurable optical devices. With the manipulation of trains of femtosecond pulses, the complex refractive index of the phase-change material (GST) converts from its amorphous state to the crystalline state, allowing GST films to be written with high accuracy. d) Calculated electric energy intensity of a micro-lens in the *x*–*z* plane. Insets: SEM image of a-Si posts (upper) and the real part of the *z* component of the Poynting vector at the plane of focus (lower). e) Left panel: measured full width at half maximum (FWHM) of the spot size, transmission, and focusing efficiency of micro-lenses as a function of focusing distance, *d*. Right panel: the spectra of FWHM spot size and focusing efficiency when the focusing distance of micro-lens is 175 μm. f,g) Design procedure of conformal metasurfaces demonstrated by using a converging cylinder (f) and a diverging cylinder (g) as the wrapped object. Left panels show the calculated optical path difference (OPD) of the rays transmitted through the non-planar objects. Right panels display the desired OPD along the surface of the object. The conformal metasurfaces at the surface of the nonplanar object can thus be designed according to the phase difference between the original and desired profiles (middle panels). a) Reproduced with permission.[85] Copyright 2016, American Association for the Advancement of Science. b) Reproduced with permission.[87] Copyright 2015, American Chemical Society. c) Reproduced with permission.[62] Copyright 2016, Nature Publishing Group. d,e) Reproduced with permission.[49] Copyright 2015, Nature Publishing Group. f,g) Reproduced with permission.[47] Copyright 2016, Nature Publishing Group.

also face the same problem because of the intrinsic dispersive behavior of the resonators, thus degrading the performance of an imaging system.[88,89] To eliminate chromatic aberration, Capasso's group proposed the concept of the achromatic metalens, which imparts a wavelength-dependent phase contribution to compensate the dispersive accumulated phase through light propagation. They realized an achromatic metalens operating at telecom wavelengths by using an aperiodic arrangement of coupled rectangular dielectric resonators (Figure 9b).[88,87] This design allows the incident near-infrared light to have the same focal lengths at three designed wavelengths of 1300, 1550, and 1800 nm.

Wang et al. demonstrated randomly reconfigurable metasurface devices by writing, erasing, and rewriting 2D grayscale or binary patterns into a phase-change material ($Ge_2Sb_2Te_5$, GST) (Figure 9c).[62] They demonstrated chromatically selective and chromatically corrected lenses by writing binary and grayscale Fresnel zone-plate patterns in GST thin film. Via careful control of the energy and the repetition rate of a femtosecond laser, the reversible refractive-index phase transition of GST can be

applied to perform the write–erase–write reconfigurable cycle of Fresnel zone-plate patterns.

Faraon's group theoretically and experimentally demonstrated polarization-insensitive and high-numerical-aperture lenses with measured focusing efficiency as large as 82% at telecom wavelengths (Figure 9d,e).[49] These metalenses were based on high-contrast metasurfaces, composed of high-refractive-index amorphous silicon (a-Si) nanoposts on a glass substrate. Despite the planar substrates, such high-transmittance arrays can also be applied to arbitrarily nonplanar-shaped objects and dramatically alter their original optical property. As shown in Figure 9f,g, the cylinder-shaped lenses were demonstrated to functionalize as aspherical lenses by covering them with designed metasurfaces, displaying over 50% focusing efficiency in the near-infrared.[47]

4.2.2. Metaholograms

Another interesting platform of metasurfaces would be the realization of computer-generated holograms (CGHs), which requires careful engineering of local phase, amplitude, and polarization response in order to get high-quality images. Complementary V-shaped structures have been utilized to introduce an eight-level phase and a two-level amplitude distribution for the reconstruction of a holographic image in visible light with efficiency of 10%.[90] PB-phase metasurfaces or geometric metasurfaces have also been widely used for the design of metaholograms due to their superior phase control.[91–95] For example, three-dimensional (3D) optical holography[91,96] has been demonstrated to project an on-axis 3D jet-shaped image with a wide FOV evaluated as ±40° (**Figure 10**a). The required phase profile of this design is imparted via the rotation angles of the subwavelength gold nanorods. To enhance image-conversion efficiency, Zhang's group further used a multilayer design by introducing a ground metallic plane to the PB-phase metasurfaces.[93] Similar to the concept of metasurface-based reflective half-wave plates, the fast- and slow-axis resonances of each nanorod are designed to have a phase delay of π for optimizing the conversion efficiency between the two CP states. The reconstructed 16-level-phase CGHs achieve diffraction efficiency over 50% in a broad bandwidth of 630–1050 nm with a maximum of 80% at 825 nm (Figure 10b).[93]

Recently, such highly efficient and broadband reflective-type configurations were further applied to helicity-multiplexed metaholograms. Wen et al. used two sets of reflective PB phase metasurfaces to independently sample two hologram patterns with 16-phase levels projecting into the left and right sides of incoming CP light beams, respectively. These two metaholograms were then combined by an interlaced arrangement of nanorod arrays. As shown in Figure 10c, the positions of the reconstructed symmetrical off-axis holographic images can be exchanged by altering the handedness of the input wave.[94] The measured conversion efficiency in this work could reach more than 40% from 620 to 1020 nm. Khorasaninejad et al., on the other hand, utilized geometric metasurfaces consisting of two sets of rotated Si nanofin arrays in each pixel to project different letters along the same direction when switching the helicity of incident CP light beams (Figure 10d).[95]

In addition to helicity-multiplexed holograms, polarization-multiplexed metaholograms operating in LP light illumination were also demonstrated.[96,98,97] For example, Montelongo et al. utilized both vertically and horizontally orientated silver nanorods with an L-shaped arrangement to display polarization-switchable metaholograms (Figure 10e).[97] Tsai's group fabricated cross-shaped gold nanorods with size variations to construct a four-phase-level CGH that exhibited two distinct images when illuminated by orthogonal LP light (Figure 10f).[98] Li et al. used graphene oxides through an athermal photoreduction process to write the required phase variation for 3D vectorial metaholograms carrying polarization-sensitive information (Figure 10g).[96] The recent development also includes several examples demonstrating polarization-insensitive holograms.[99–101,104] For example, Huang et al. fabricated an ultrahigh density of nanoholes randomly distributed in a chromium film to demonstrate a metahologram with diffraction efficiency up to 47% (Figure 10h).[99] Kivshar's group employed high-refractive-index Si nanodisks with different lattice periodicities to construct a four-level phase mask, which generated a visually identical holographic image of "*hv*" with 40% imaging efficiency for horizontal and vertical polarizations in the near-infrared (Figure 10i).[100] Their recent work has further exploited Si nanopillars with 36 different radii to demonstrate two holographic patterns with a measured transmission efficiency up to 90% and diffraction efficiency over 99% at 1600 nm (Figure 10j).[101]

Another aspect of recent developments would be the manipulation of phases at dual[105–107] or triple wavelengths[96,102,103] to achieve full-color metaholograms. For example, Tsai's group demonstrated a multicolor hologram utilizing Al nanorods with different sizes to form a two-level phase modulation at three primary colors (Figure 10k).[102] Wang et al. used three different sizes of Si nanoblocks with subwavelength spacing and changed the in-phase orientations of each nanoblock to achieve full phase control for red, green, and blue wavelengths.[103] Two different functional color holograms were demonstrated, where the achromatic metahologram generated identical images for all three wavelengths, and the highly dispersive metahologram projected distinct images at specific wavelengths (Figure 10l).

4.2.3. Optical Vortex Generation

Metasurface-based devices applied to vortex-beam generation have recently gained tremendous interest due to their various promising applications in high-resolution microscopy, optical tweezers, and classical and quantum communication technology.[108,109] A variety of plasmonic nanostructures such as the plasmonic Archimedes' spiral[108–112] and plasmonic rings[113–115] have been demonstrated in generating either vectorial or scalar vortex beams with arbitrary orbital angular momentum (OAM) values. On the other hand, PB-phase metasurfaces consisting of nanoantennas possessing rotation surrounding the origin can also be used for optical vortex generation, where the rotational rate of the nanoantennas across one circumference determines the topological charge of the structure.[78,116–119] For example, a metasurface composed of nanoantennas possessing one full rotation of 360° surrounding the origin corresponds to a topological

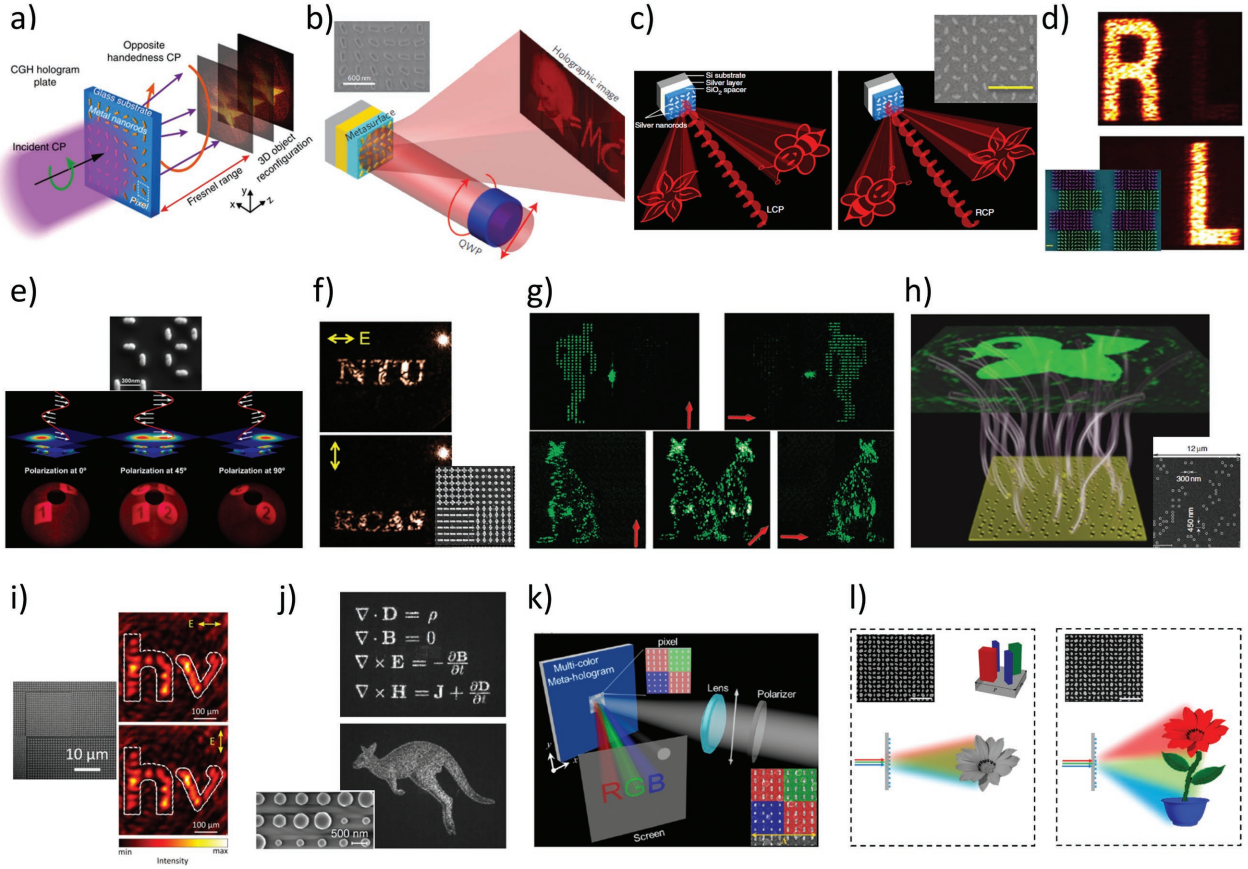

Figure 10. a) 3D holography consisting of subwavelength metallic nanorods with spatially varying orientations generates an on-axis jet image upon normal incidence of CP light. b) Schematic illustration of the working principle of a highly efficient reflective hologram employing a PB-phase metasurface combined with a back metallic plane. The inset shows an SEM image of the fabricated metasurface. c) Diagram of a helicity-multiplexed hologram realized by a reflective PB-phase metasurface. The inset shows an SEM image of part of the fabricated sample. d) A helicity-multiplexed metahologram shows letters of "R" and "L," respectively, upon RCP and LCP light illumination. The inset shows a false-colored SEM image of part of the fabricated sample consisting of two parts (green and purple) in each pixel. e) A polarization-switchable metahologram showing two independent patterns at 0° and 90° polarization. The inset displays an SEM image of the fabricated metasurface consisting of horizontally and vertically oriented nanorods arranged in an L shape. f) Two distinct reconstructed images of a polarization-multiplexed hologram generated at the horizontal and vertical polarization angles. Inset: an SEM image of the fabricated sample consisting of cross-shaped nanoantennas. g) The reconstruction of a 3D vectorial wavefront based on athermally photoreduced graphene oxides. h) A polarization-insensitive metahologram made of ultrahigh-capacity aperiodic nanoholes. Inset: SEM image of part of the fabricated sample. i) Holographic images generated by horizontally and vertically polarized light are visually identical. Inset: SEM image of part of the fabricated dielectric Huygens' metasurfaces. j) High transmission and diffraction efficiency metaholograms with the inset showing an SEM image of the fabricated Si nanopillar arrays. k) Sketch of multicolor holograms using Al nanorods as the basic building block. Inset: SEM image of one pixel of the hologram with the colored area indicating the four subpixels. l) Left panel: an achromatic metahologram generates the same image of a flower for three primary colors. Left and right insets: SEM image of part of the fabricated sample and the basic building block consisting of three differently sized Si nanoblocks with in-plane PB phase orientations, respectively. Right panel: a highly dispersive metahologram projects a triple colored image of a red flower, a green peduncle, and a blue pot. The inset shows an SEM image of a portion of the fabricated sample. a) Reproduced with permission.[91] Copyright 2013, Nature Publishing Group. b) Reproduced with permission.[93] Copyright 2015, Nature Publishing Group. c) Reproduced with permission.[94] Copyright 2015, Nature Publishing Group. d) Reproduced with permission.[95] Copyright 2016, American Association for the Advancement of Science. e) Reproduced with permission.[97] Copyright 2014, American Chemical Society. f) Reproduced with permission.[98] Copyright 2014, American Chemical Society. g) Reproduced with permission.[96] Copyright 2015, Nature Publishing Group. h) Reproduced with permission.[99] Copyright 2015, Nature Publishing Group. i) Reproduced with permission.[100] Copyright 2016, American Chemical Society. j) Reproduced with permission.[101] Copyright 2016, Optical Society of America. k) Reproduced with permission.[102] Copyright 2015, American Chemical Society. l) Reproduced with permission.[103] Copyright 2016, American Chemical Society.

charge of $q = 1$ (**Figure 11**a). Owing to its rotationally invariant property, this metasurface does not exchange angular momentum with the optical field. However, since the handednesses of the input and output beams are not identical, the conservation of angular momentum suggests that the change in the spin-angular momentum must be transformed into OAM. Therefore, this device yields light carrying OAM of $l = \pm 2q\hbar$.[116,117]

As rotational symmetry is not a requirement for spin-to-OAM conversion, Boyd's group fabricated metasurfaces that are capable of generating OAM with values varying from −25 to 25 with a conversion efficiency of 9% at 760–790 nm (Figure 11b).[117] Recently, Zeng et al. further fabricated a gradient-rotation split-ring antenna metasurface containing the superposition of both linear-gradient phase and rotation-spiral

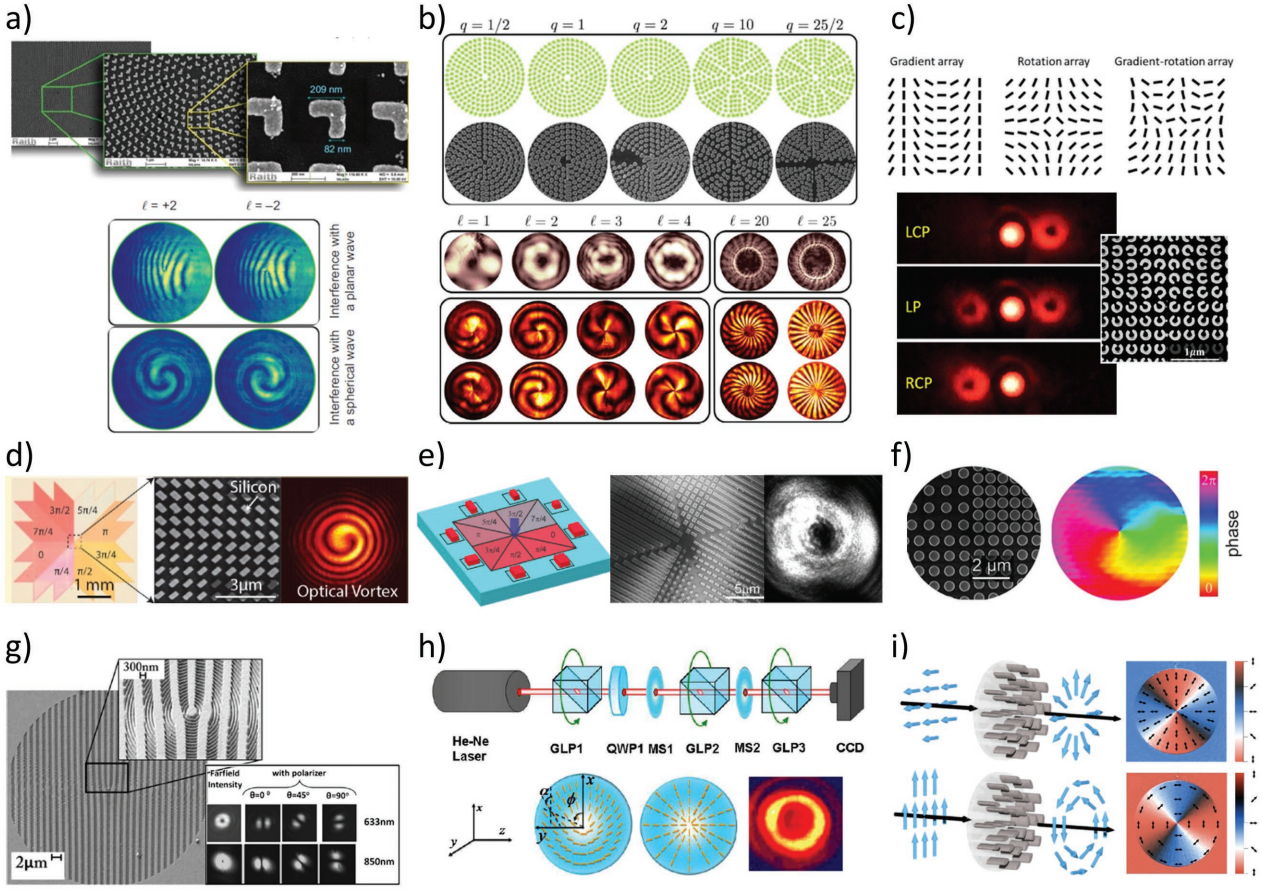

Figure 11. a) Upper panel: SEM image of a fabricated metasurface with topological charge of 1. Lower panel: interference patterns of the converted vortex beams with planer (upper) and spherical (lower) waves. b) Upper panel: designed spatial arrangement of nanoantennas and their corresponding SEM images for generating output beams carrying OAM values of (±1, ±2, ±4, ±20, and ±25). Lower panel: intensity profiles of the object beams and their interference patterns with a spherical wave. c) Upper panel: schematics of the orientation distributions of nanorod arrays for achieving gradient phase, rotation phase, and gradient-rotation phase, respectively. The gradient-rotation phase is the superposition of the linear-gradient phase and the rotational-spiral phase. Lower panel: measured transmitted diffraction images of gradient-rotation arrays that demonstrate that the converted vortex beams are bent to designed diffraction angles under CP light illumination. Inset: an SEM image of the gradient-rotation arrays made of split-ring antennas. d) Optical microscopy image of a dielectric meta-reflectarray with a spiral phase profile ranging for 0 to 2π. Left inset: SEM image of eight Si cut-wire resonators showing a constant phase difference $\Delta\Phi = \pi/4$ along the azimuthal direction. Right inset: interference pattern of the generated vortex beam with a Gaussian beam. e) Schematic illustration (left panel) and SEM image (middle panel) of a spiral phase plate based on dielectric Huygens' metasurfaces. Right panel: intensity distribution of measured output beam. f) Left panel: SEM image of a fabricated polarization-independent optical vortex beam converter based on dielectric Huygens' metasurfaces. Right panel: reconstructed phase of the generated vortex beam. g) Left panel: SEM micrograph of a holographic interface for generating vector beams with inset showing higher magnification. Right panel: measured far-field intensity distributions at 633 and 850 nm. The distinct features with respect to different rotation angles of the linear polarizer reveal the radially polarized characteristic. h) Experimental setup for vector beams generation by two cascaded metasurfaces. The bottom insets show sketches of metasurfaces with $q = 0.5$ and $q = 1$, respectively, and intensity distributions of the generated vector beams. i) Schematic view of high-transmission vectorial vortex-beam converter based on dielectric Huygens' metasurfaces and the corresponding measured polarization distribution of the output beams. Upper panel: the conversion of linear horizontal polarization to radial polarization. Lower panel: the conversion of linear vertical polarization to azimuthal polarization. a) Reproduced with permission.[116] Copyright 2014, Nature Publishing Group. b) Reproduced with permission.[117] Copyright 2014, American Institute of Physics. c) Reproduced with permission.[120] Copyright 2016, American Chemical Society. d) Reproduced with permission.[121] Copyright 2014, American Chemical Society. e) Reproduced with permission.[122] Copyright 2015, American Chemical Society. f) Reproduced with permission.[123] Copyright 2015, American Chemical Society. g) Reproduced with permission.[124] Copyright 2013, American Chemical Society. h) Reproduced with permission.[125] Copyright 2014, Optical Society of America. i) Reproduced with permission.[39] Copyright 2016, American Chemical Society.

Table 3. Summary of previously reported half-wave plates.

Functionality	Reflective terahertz HWP[73]	Transmitted terahertz HWP[73]	Transmitted terahertz HWP[74]	Reflective near-infrared HWP[72]	Reflective HWP[69]
Cross-polarized reflectance/ transmission	0.73–1.8 THz: >80% Max. at 1.36 THz: 88%	0.52–1.82 THz: >50% Max. at 1.04 THz: 80%	0.2–0.35 THz: > 85%	1100–1700 nm: >65%	640–1290 nm: >92%

Table 4. Summary of previously reported metalenses.

Functionality	Mechanisms	Operation wavelength/focusing efficiency (FWHM spot size)
Metalenses at visible wavelengths[85]	Dielectric PB phase metasurfaces	405 nm: 86% (0.68λ)
		532 nm: 73% (0.70λ)
		660 nm: 66% (0.69λ)
Polarization-insensitive metalenses at telecommwavelengths[49]	High-contrast metasurfaces	1550 nm: 82% (2.4λ)
		1550 nm: 42% (0.57λ)
Vortex metalenses at infrared wavelengths[81]	High-contrast metasurfaces	850 nm: 70% (10λ)
Achromatic metalenses at telecom wavelengths[87]	Dielectric metasurfaces	1300 nm: 15% (21.15λ)
		1550 nm: 10% (18.71λ)
		1800 nm: 21% (13.89λ)

phase to achieve a background-free converted vortex beam with high mode purity over a broad visible range (Figure 11c).[120]

In addition to PB-phase metasurfaces, the spiral-phase profile can be achieved by properly engineering the geometry of nanoantennas.[5,123,122,121] Valentine's group used Si nanoblock resonators placed above a silver ground plane to demonstrate a high-efficiency vortex-beam generation from 1500 nm to 1600 nm (Figure 11d).[121] Shalaev et al.[122] and Kivshar's group[123] utilized all-dielectric Si Huygens' metasurfaces for vortex converters with transmission efficiency of 45% and 70%, respectively, at telecom wavelengths, as shown in Figure 11e,f.

Capasso's group combined a fork hologram and concentric circular rings to create a spiral phase front with radial polarization over a broad visible range (Figure 11g).[124] Yi et al. used two cascading metasurfaces with topological charges of $q = 0.5$ and $q = 1$ to generate cylindrical vector vortex beams. The first element was used as a spin-to-orbital angular-momentum converter, and the second was applied to manipulate the local polarization (Figure 11h).[125] Recently, Kruk et al. utilized all-dielectric Huygens' metasurfaces to convert vertical LP beams into azimuthal polarization and horizontal LP beams into radial polarization with up to 99% polarization conversion efficiency and 90% transmission at telecomm frequencies (Figure 11i).[39]

5. Conclusions and Outlook

The field of optical metasurfaces has been in rapid progress as a platform for numerous novel optical effects and potential applications.[126–128] We have reviewed a few of the representative demonstrations of metasurface-based devices such as wave plates, polarimetries, metalenses, metaholograms, and optical vortex converters, and these examples are listed in **Table 3–6**. There are still many other aspects or applications not included here, such as nonlinear metasurfaces,[129–141] hyperbolic metasurfaces,[142–148] thin-film metasurfaces,[149–155] parity–time symmetry metasurfaces,[156–159] etc. Thanks to the advances in nanofabrication technologies, these low-cost, large-area, and mass-productive techniques have sped up the development of static metadevices and are gradually becoming mature. We believe that a variety of emerging techniques and clever designs can also be adopted for metasurfaces, such as scanning probe lithography,[160–162] laser direct writing,[163–165] laser-induced forward transfer,[166–168] the multilayer electroplating technique,[169,170] multiphoton lithography,[171–173] nanostencil lithography,[174] phase-shifting photolithography,[175] shadow-mask lithography[176,177] etc. With the incorporation of functional materials, tunable or reconfigurable[41,55–59,61–63,178–189] metasurfaces further bring more exciting and versatile

Table 5. Summary of previously reported metaholograms.

Functionality	Transmitted/reflective type	Number of phase levels	Mechanisms	Operation wavelength/conversion efficiency
High-efficiency metaholograms[93]	Reflective	16	PB-phase metasurfaces	630–1050 nm: >50%
				Max. at 825 nm: 80%
Helicity-multiplexed metaholograms[94]	Reflective	16	PB-phase metasurfaces	620–1020 nm: > 40%
				Max. at 860 nm: 59.2%
Polarization- multiplexed metaholograms[98]	Reflective	4	Gap-plasmon metasurfaces	632.8 nm: 10%
				780 nm: 18%
Polarization-insensitive metaholograms[100]	Transmitted	4	Dielectric Huygens' metasurfaces	1477 nm: 40%
Polarization-insensitive metaholograms[101]	Transmitted	36	Dielectric Huygens' metasurfaces	1600 nm: 90%
Multicolor-multiplexed metaholograms[103]	Transmitted	8	Dielectric PB-phase metasurfaces	633 nm: 18%
				532 nm: 5.2%
				473 nm: 3.6%

Table 6. Summary of previously reported scalar optical vortex converters.

Functionality	Transmitted/ reflective type	Number of phase levels	Mechanisms	Operation wavelength/ conversion efficiency
Spin-to-orbital angular momentum converter[117]	Transmitted	6	Plasmonic PB-phase metasurfaces	780 nm: 8.6% ± 0.4%.
Broadband vortex-beam converter[121]	Reflective	8	Dielectric multi-resonance metasurfaces	1550 nm: 94.5%
Vortex-beam converter in transmission mode[122]	Transmitted	8	Dielectric Huygens' metasurfaces	1550 nm: 45%
Polarization-independent vortex-beam converter[123]	Transmitted	4	Dielectric Huygens' metasurfaces	1490 nm: 70%
High-purity vortex-beam converter[120]	Transmitted	4	PB-phase metasurfaces	880 nm: 6%

functionalities for broader applications. The continuous innovation of novel concepts and applications make this field still vivid and prosperous.

Acknowledgements

The authors acknowledge financial support from Ministry of Science and Technology, Taiwan (Grant No. MOST-105-2745-M-002-005-ASP and MOST 105-2811-M-002-061) and Academia Sinica (Grant No. AS-103-TP-A06). They are also grateful to National Center for Theoretical Sciences, NEMS Research Center of National Taiwan University, National Center for High-Performance Computing, Taiwan, and Research Center for Applied Sciences, Academia Sinica, Taiwan for their support.

Received: December 31, 2016
Revised: January 22, 2017
Published online: March 24, 2017

[1] N. I. Zheludev, Y. S. Kivshar, *Nat. Mater.* **2012**, *11*, 917.
[2] W. Cai, U. K. Chettiar, A. V. Kildishev, V. M. Shalaev, *Nat. Photonics* **2007**, *1*, 224.
[3] J. B. Pendry, D. Schurig, D. R. Smith, *Science* **2006**, *312*, 1780.
[4] C. M. Soukoulis, M. Wegener, *Science* **2010**, *330*, 1633.
[5] N. Yu, P. Genevet, M. A. Kats, F. Aieta, J.-P. Tetienne, F. Capasso, Z. Gaburro, *Science* **2011**, *334*, 333.
[6] N. Yu, F. Capasso, *Nat. Mater.* **2014**, *13*, 139.
[7] G. Patrice, C. Federico, *Rep. Prog. Phys.* **2015**, *78*, 024401.
[8] S. B. Glybovski, S. A. Tretyakov, P. A. Belov, Y. S. Kivshar, C. R. Simovski, *Phys. Rep.* **2016**, *634*, 1.
[9] L. Zhang, S. Mei, K. Huang, C.-W. Qiu, *Adv. Opt. Mater.* **2016**, *4*, 818.
[10] N. M. Estakhri, A. Alù, *J. Opt. Soc. Am. B* **2016**, *33*, A21.
[11] A. V. Kildishev, A. Boltasseva, V. M. Shalaev, *Science* **2013**, *339*, 1289.
[12] N. Meinzer, W. L. Barnes, I. R. Hooper, *Nat. Photonics* **2014**, *8*, 889.
[13] A. E. Minovich, A. E. Miroshnichenko, A. Y. Bykov, T. V. Murzina, D. N. Neshev, Y. S. Kivshar, *Laser Photonics Rev.* **2015**, *9*, 195.
[14] A. M. Shaltout, A. V. Kildishev, V. M. Shalaev, *J. Opt. Soc. Am. B* **2016**, *33*, 501.
[15] F. Aieta, P. Genevet, N. Yu, M. A. Kats, Z. Gaburro, F. Capasso, *Nano Lett.* **2012**, *12*, 1702.
[16] C. Hou-Tong, J. T. Antoinette, Y. Nanfang, *Rep. Prog. Phys.* **2016**, *79*, 076401.
[17] N. Yu, P. Genevet, F. Aieta, M. A. Kats, R. Blanchard, G. Aoust, J. P. Tetienne, Z. Gaburro, F. Capasso, *IEEE J. Sel. Top. Quantum Electron.* **2013**, *19*, 4700423.
[18] R. Blanchard, G. Aoust, P. Genevet, N. Yu, M. A. Kats, Z. Gaburro, F. Capasso, *Phys. Rev. B* **2012**, *85*, 155457.
[19] N. Yu, F. Aieta, P. Genevet, M. A. Kats, Z. Gaburro, F. Capasso, *Nano Lett.* **2012**, *12*, 6328.
[20] X. Ni, N. K. Emani, A. V. Kildishev, A. Boltasseva, V. M. Shalaev, *Science* **2012**, *335*, 427.
[21] S. Sun, K.-Y. Yang, C.-M. Wang, T.-K. Juan, W. T. Chen, C. Y. Liao, Q. He, S. Xiao, W.-T. Kung, G.-Y. Guo, L. Zhou, D. P. Tsai, *Nano Lett.* **2012**, *12*, 6223.
[22] S. Sun, Q. He, S. Xiao, Q. Xu, X. Li, L. Zhou, *Nat. Mater.* **2012**, *11*, 426.
[23] C. Pfeiffer, A. Grbic, *Phys. Rev. Lett.* **2013**, *110*, 197401.
[24] F. Monticone, N. M. Estakhri, A. Alù, *Phys. Rev. Lett.* **2013**, *110*, 203903.
[25] A. Pors, S. I. Bozhevolnyi, *Opt. Express* **2013**, *21*, 27438.
[26] W. Mo, X. Wei, K. Wang, Y. Li, J. Liu, *Opt. Express* **2016**, *24*, 13621.
[27] L. Zhang, J. Hao, M. Qiu, S. Zouhdi, J. K. W. Yang, C.-W. Qiu, *Nanoscale* **2014**, *6*, 12303.
[28] W.-L. Hsu, P. C. Wu, J.-W. Chen, T.-Y. Chen, B. H. Cheng, W. T. Chen, Y.-W. Huang, C. Y. Liao, G. Sun, D. P. Tsai, *Sci. Rep.* **2015**, *5*, 11226.
[29] A. Pors, M. G. Nielsen, R. L. Eriksen, S. I. Bozhevolnyi, *Nano Lett.* **2013**, *13*, 829.
[30] A. Pors, O. Albrektsen, I. P. Radko, S. I. Bozhevolnyi, *Sci. Rep.* **2013**, *3*, 2155.
[31] L. Huang, X. Chen, H. Mühlenbernd, G. Li, B. Bai, Q. Tan, G. Jin, T. Zentgraf, S. Zhang, *Nano Lett.* **2012**, *12*, 5750.
[32] S.-C. Jiang, X. Xiong, Y.-S. Hu, S.-W. Jiang, Y.-H. Hu, D.-H. Xu, R.-W. Peng, M. Wang, *Phys. Rev. B* **2015**, *91*, 125421.
[33] L. Cong, N. Xu, W. Zhang, R. Singh, *Adv. Opt. Mater.* **2015**, *3*, 1176.
[34] X. Chen, L. Huang, H. Mühlenbernd, G. Li, B. Bai, Q. Tan, G. Jin, C.-W. Qiu, S. Zhang, T. Zentgraf, *Nat. Commun.* **2012**, *3*, 1198.
[35] M. Kang, T. Feng, H.-T. Wang, J. Li, *Opt. Express* **2012**, *20*, 15882.
[36] D. Wen, F. Yue, S. Kumar, Y. Ma, M. Chen, X. Ren, P. E. Kremer, B. D. Gerardot, M. R. Taghizadeh, G. S. Buller, X. Chen, *Opt. Express* **2015**, *23*, 10272.
[37] X. Ding, F. Monticone, K. Zhang, L. Zhang, D. Gao, S. N. Burokur, A. de Lustrac, Q. Wu, C.-W. Qiu, A. Alù, *Adv. Mater.* **2015**, *27*, 1195.
[38] C. Pfeiffer, N. K. Emani, A. M. Shaltout, A. Boltasseva, V. M. Shalaev, A. Grbic, *Nano Lett.* **2014**, *14*, 2491.
[39] S. Kruk, B. Hopkins, I. I. Kravchenko, A. Miroshnichenko, D. N. Neshev, Y. S. Kivshar, *APL Photonics* **2016**, *1*, 030801.
[40] M. Decker, I. Staude, M. Falkner, J. Dominguez, D. N. Neshev, I. Brener, T. Pertsch, Y. S. Kivshar, *Adv. Opt. Mater.* **2015**, *3*, 813.
[41] P. P. Iyer, N. A. Butakov, J. A. Schuller, *ACS Photonics* **2015**, *2*, 1077.
[42] U. Zywietz, A. B. Evlyukhin, C. Reinhardt, B. N. Chichkov, *Nat. Commun.* **2014**, *5*, 3402.
[43] A. I. Kuznetsov, A. E. Miroshnichenko, M. L. Brongersma, Y. S. Kivshar, B. Luk'yanchuk, *Science* **2016**, *354*, 846.
[44] S. Jahani, Z. Jacob, *Nat. Nanotechnol.* **2016**, *11*, 23.

[45] Y. H. Fu, A. I. Kuznetsov, A. E. Miroshnichenko, Y. F. Yu, B. Luk'yanchuk, *Nat. Commun.* **2013**, *4*, 1527.
[46] Y. F. Yu, A. Y. Zhu, R. Paniagua-Domínguez, Y. H. Fu, B. Luk'yanchuk, A. I. Kuznetsov, *Laser Photonics Rev.* **2015**, *9*, 412.
[47] S. M. Kamali, A. Arbabi, E. Arbabi, Y. Horie, A. Faraon, *Nat. Commun.* **2016**, *7*, 11618.
[48] A. Arbabi, Y. Horie, M. Bagheri, A. Faraon, *Nat. Nanotechnol.* **2015**, *10*, 937.
[49] A. Arbabi, Y. Horie, A. J. Ball, M. Bagheri, A. Faraon, *Nat. Commun.* **2015**, *6*, 7069.
[50] Z. J. Zhang, J. Luo, M. W. Song, H. L. Yu, *Appl. Phys. Lett.* **2015**, *107*, 241904.
[51] J. Y. Kim, H. Kim, B. H. Kim, T. Chang, J. Lim, H. M. Jin, J. H. Mun, Y. J. Choi, K. Chung, J. Shin, S. Fan, S. O. Kim, *Nat. Commun.* **2016**, *7*, 12911.
[52] W. Chen, M. Tymchenko, P. Gopalan, X. Ye, Y. Wu, M. Zhang, C. B. Murray, A. Alu, C. R. Kagan, *Nano Lett.* **2015**, *15*, 5254.
[53] R. Verre, M. Svedendahl, N. O. Lank, Z. J. Yang, G. Zengin, T. J. Antosiewicz, M. Kall, *Nano Lett.* **2016**, *16*, 98.
[54] C. Lu, R. H. Lipson, *Laser Photonics Rev.* **2010**, *4*, 568.
[55] P. Gutruf, C. J. Zou, W. Withayachumnankul, M. Bhaskaran, S. Sriram, C. Fumeaux, *ACS Nano* **2016**, *10*, 133.
[56] H. S. Ee, R. Agarwal, *Nano Lett.* **2016**, *16*, 2818.
[57] J. Sautter, I. Staude, M. Decker, E. Rusak, D. N. Neshev, I. Brener, Y. S. Kivshar, *ACS Nano* **2015**, *9*, 4308.
[58] O. Buchnev, N. Podoliak, M. Kaczmarek, N. I. Zheludev, V. A. Fedotov, *Adv. Opt. Mater.* **2015**, *3*, 674.
[59] M. R. M. Hashemi, S.-H. Yang, T. Wang, N. Sepúlveda, M. Jarrahi, *Sci. Rep.* **2016**, *6*, 35439.
[60] D. Wang, L. Zhang, Y. Gong, L. Jian, T. Venkatesan, C. W. Qiu, M. Hong, *IEEE Photonics J.* **2016**, *8*, 5500308.
[61] D. Wang, L. Zhang, Y. Gu, M. Q. Mehmood, Y. Gong, A. Srivastava, L. Jian, T. Venkatesan, C.-W. Qiu, M. Hong, *Sci. Rep.* **2015**, *5*, 15020.
[62] Q. Wang, E. T. F. Rogers, B. Gholipour, C.-M. Wang, G. Yuan, J. Teng, N. I. Zheludev, *Nat. Photonics* **2016**, *10*, 60.
[63] N. Dabidian, I. Kholmanov, A. B. Khanikaev, K. Tatar, S. Trendafilov, S. H. Mousavi, C. Magnuson, R. S. Ruoff, G. Shvets, *ACS Photonics* **2015**, *2*, 216.
[64] W. M. Zhu, Q. H. Song, L. B. Yan, W. Zhang, P. C. Wu, L. K. Chin, H. Cai, D. P. Tsai, Z. X. Shen, T. W. Deng, S. K. Ting, Y. D. Gu, G. Q. Lo, D. L. Kwong, Z. C. Yang, R. Huang, A. Q. Liu, N. Zheludev, *Adv. Mater.* **2015**, *27*, 4739.
[65] D. Wen, S. Chen, F. Yue, K. Chan, M. Chen, M. Ardron, K. F. Li, P. W. H. Wong, K. W. Cheah, E. Y. B. Pun, G. Li, S. Zhang, X. Chen, *Adv. Opt. Mater.* **2016**, *4*, 321.
[66] B. Yang, W.-M. Ye, X.-D. Yuan, Z.-H. Zhu, C. Zeng, *Opt. Lett.* **2013**, *38*, 679.
[67] Y. Zhao, A. Alù, *Nano Lett.* **2013**, *13*, 1086.
[68] C. Wu, N. Arju, G. Kelp, J. A. Fan, J. Dominguez, E. Gonzales, E. Tutuc, I. Brener, G. Shvets, *Nat. Commun.* **2014**, *5*, 3892.
[69] Z. H. Jiang, L. Lin, D. Ma, S. Yun, D. H. Werner, Z. Liu, T. S. Mayer, *Sci. Rep.* **2014**, *4*, 7511.
[70] Z. Li, W. Liu, H. Cheng, S. Chen, J. Tian, *Sci. Rep.* **2015**, *5*, 18106.
[71] D. Wang, Y. Gu, Y. Gong, C.-W. Qiu, M. Hong, *Opt. Express* **2015**, *23*, 11114.
[72] F. Ding, Z. Wang, S. He, V. M. Shalaev, A. V. Kildishev, *ACS Nano* **2015**, *9*, 4111.
[73] N. K. Grady, J. E. Heyes, D. R. Chowdhury, Y. Zeng, M. T. Reiten, A. K. Azad, A. J. Taylor, D. A. R. Dalvit, H.-T. Chen, *Science* **2013**, *340*, 1304.
[74] R.-H. Fan, Y. Zhou, X.-P. Ren, R.-W. Peng, S.-C. Jiang, D.-H. Xu, X. Xiong, X.-R. Huang, M. Wang, *Adv. Mater.* **2015**, *27*, 1201.
[75] A. Shaltout, J. Liu, A. Kildishev, V. Shalaev, *Optica* **2015**, *2*, 860.
[76] A. Shaltout, J. Liu, V. M. Shalaev, A. V. Kildishev, *Nano Lett.* **2014**, *14*, 4426.
[77] P. C. Wu, W.-Y. Tsai, W. T. Chen, Y.-W. Huang, T.-Y. Chen, J.-W. Chen, C. Y. Liao, C. H. Chu, G. Sun, D. P. Tsai, *Nano Lett.* **2017**, *17*, 445.
[78] Y. Liu, X. Ling, X. Yi, X. Zhou, S. Chen, Y. Ke, H. Luo, S. Wen, *Opt. Lett.* **2015**, *40*, 756.
[79] A. Pors, M. G. Nielsen, S. I. Bozhevolnyi, *Optica* **2015**, *2*, 716.
[80] W. T. Chen, P. Török, M. R. Foreman, C. Y. Liao, W. Y. Tsai, P. R. Wu, D. P. Tsai, *Nanotechnology* **2016**, *27*, 224002.
[81] S. Vo, D. Fattal, W. V. Sorin, Z. Peng, T. Tran, M. Fiorentino, R. G. Beausoleil, *IEEE Photonics Technol. Lett.* **2014**, *26*, 1375.
[82] F. Aieta, P. Genevet, M. A. Kats, N. Yu, R. Blanchard, Z. Gaburro, F. Capasso, *Nano Lett.* **2012**, *12*, 4932.
[83] X. Ni, S. Ishii, A. V. Kildishev, V. M. Shalaev, *Light Sci. Appl.* **2013**, *2*, e72.
[84] D. Lin, P. Fan, E. Hasman, M. L. Brongersma, *Science* **2014**, *345*, 298.
[85] M. Khorasaninejad, W. T. Chen, R. C. Devlin, J. Oh, A. Y. Zhu, F. Capasso, *Science* **2016**, *352*, 1190.
[86] M. Khorasaninejad, W. T. Chen, A. Y. Zhu, J. Oh, R. C. Devlin, D. Rousso, F. Capasso, *Nano Lett.* **2016**, *16*, 4595.
[87] M. Khorasaninejad, F. Aieta, P. Kanhaiya, M. A. Kats, P. Genevet, D. Rousso, F. Capasso, *Nano Lett.* **2015**, *15*, 5358.
[88] F. Aieta, M. A. Kats, P. Genevet, F. Capasso, *Science* **2015**, *347*, 1342.
[89] E. Arbabi, A. Arbabi, S. M. Kamali, Y. Horie, A. Faraon, *Optica* **2016**, *3*, 628.
[90] X. Ni, A. V. Kildishev, V. M. Shalaev, *Nat. Commun.* **2013**, *4*, 2807.
[91] L. Huang, X. Chen, H. Mühlenbernd, H. Zhang, S. Chen, B. Bai, Q. Tan, G. Jin, K.-W. Cheah, C.-W. Qiu, J. Li, T. Zentgraf, S. Zhang, *Nat. Commun.* **2013**, *4*, 2808.
[92] X. Zhang, J. Jin, Y. Wang, M. Pu, X. Li, Z. Zhao, P. Gao, C. Wang, X. Luo, *Sci. Rep.* **2016**, *6*, 19856.
[93] G. Zheng, H. Mühlenbernd, M. Kenney, G. Li, T. Zentgraf, S. Zhang, *Nat. Nanotechnol.* **2015**, *10*, 308.
[94] D. Wen, F. Yue, G. Li, G. Zheng, K. Chan, S. Chen, M. Chen, K. F. Li, P. W. H. Wong, K. W. Cheah, E. Yue Bun Pun, S. Zhang, X. Chen, *Nat. Commun.* **2015**, *6*, 8241.
[95] M. Khorasaninejad, A. Ambrosio, P. Kanhaiya, F. Capasso, *Sci. Adv.* **2016**, *2*, e1501258.
[96] X. Li, H. Ren, X. Chen, J. Liu, Q. Li, C. Li, G. Xue, J. Jia, L. Cao, A. Sahu, B. Hu, Y. Wang, G. Jin, M. Gu, *Nat. Commun.* **2015**, *6*, 6984.
[97] Y. Montelongo, J. O. Tenorio-Pearl, W. I. Milne, T. D. Wilkinson, *Nano Lett.* **2014**, *14*, 294.
[98] W. T. Chen, K.-Y. Yang, C.-M. Wang, Y.-W. Huang, G. Sun, I. D. Chiang, C. Y. Liao, W.-L. Hsu, H. T. Lin, S. Sun, L. Zhou, A. Q. Liu, D. P. Tsai, *Nano Lett.* **2014**, *14*, 225.
[99] K. Huang, H. Liu, F. J. Garcia-Vidal, M. Hong, B. Luk'yanchuk, J. Teng, C.-W. Qiu, *Nat. Commun.* **2015**, *6*, 7059.
[100] K. E. Chong, L. Wang, I. Staude, A. R. James, J. Dominguez, S. Liu, G. S. Subramania, M. Decker, D. N. Neshev, I. Brener, Y. S. Kivshar, *ACS Photonics* **2016**, *3*, 514.
[101] L. Wang, S. Kruk, H. Tang, T. Li, I. Kravchenko, D. N. Neshev, Y. S. Kivshar, *Optica* **2016**, *3*, 1504.
[102] Y.-W. Huang, W. T. Chen, W.-Y. Tsai, P. C. Wu, C.-M. Wang, G. Sun, D. P. Tsai, *Nano Lett.* **2015**, *15*, 3122.
[103] B. Wang, F. Dong, Q.-T. Li, D. Yang, C. Sun, J. Chen, Z. Song, L. Xu, W. Chu, Y.-F. Xiao, Q. Gong, Y. Li, *Nano Lett.* **2016**, *16*, 5235.
[104] W. Zhao, H. Jiang, B. Liu, J. Song, Y. Jiang, C. Tang, J. Li, *Sci. Rep.* **2016**, *6*, 30613.
[105] B. Walther, C. Helgert, C. Rockstuhl, F. Setzpfandt, F. Eilenberger, E.-B. Kley, F. Lederer, A. Tünnermann, T. Pertsch, *Adv. Mater.* **2012**, *24*, 6300.

[106] Y. Montelongo, J. O. Tenorio-Pearl, C. Williams, S. Zhang, W. I. Milne, T. D. Wilkinson, *Proc. Natl. Acad. Sci. USA* **2014**, *111*, 12679.
[107] B. Wang, B. Quan, J. He, Z. Xie, X. Wang, J. Li, Q. Kan, Y. Zhang, *Sci. Rep.* **2016**, *6*, 35657.
[108] G. Rui, Q. Zhan, *Nanophotonics* **2015**, *4*, 2.
[109] G. Spektor, A. David, B. Gjonaj, G. Bartal, M. Orenstein, *Nano Lett.* **2015**, *15*, 5739.
[110] C.-F. Chen, C.-T. Ku, Y.-H. Tai, P.-K. Wei, H.-N. Lin, C.-B. Huang, *Nano Lett.* **2015**, *15*, 2746.
[111] W. Chen, D. C. Abeysinghe, R. L. Nelson, Q. Zhan, *Nano Lett.* **2010**, *10*, 2075.
[112] Y. Gorodetski, A. Niv, V. Kleiner, E. Hasman, *Phys. Rev. Lett.* **2008**, *101*, 043903.
[113] N. Shitrit, I. Bretner, Y. Gorodetski, V. Kleiner, E. Hasman, *Nano Lett.* **2011**, *11*, 2038.
[114] H. Kim, J. Park, S.-W. Cho, S.-Y. Lee, M. Kang, B. Lee, *Nano Lett.* **2010**, *10*, 529.
[115] A. Liu, G. Rui, X. Ren, Q. Zhan, G. Guo, G. Guo, *Opt. Express* **2012**, *20*, 24151.
[116] E. Karimi, S. A. Schulz, I. De Leon, H. Qassim, J. Upham, R. W. Boyd, *Light Sci. Appl.* **2014**, *3*, e167.
[117] F. Bouchard, I. De Leon, S. A. Schulz, J. Upham, E. Karimi, R. W. Boyd, *Appl. Phys. Lett.* **2014**, *105*, 101905.
[118] G. Li, M. Kang, S. Chen, S. Zhang, E. Y.-B. Pun, K. W. Cheah, J. Li, *Nano Lett.* **2013**, *13*, 4148.
[119] E. Maguid, I. Yulevich, D. Veksler, V. Kleiner, M. L. Brongersma, E. Hasman, *Science* **2016**, *352*, 1202.
[120] J. Zeng, L. Li, X. Yang, J. Gao, *Nano Lett.* **2016**, *16*, 3101.
[121] Y. Yang, W. Wang, P. Moitra, I. I. Kravchenko, D. P. Briggs, J. Valentine, *Nano Lett.* **2014**, *14*, 1394.
[122] M. I. Shalaev, J. Sun, A. Tsukernik, A. Pandey, K. Nikolskiy, N. M. Litchinitser, *Nano Lett.* **2015**, *15*, 6261.
[123] K. E. Chong, I. Staude, A. James, J. Dominguez, S. Liu, S. Campione, G. S. Subramania, T. S. Luk, M. Decker, D. N. Neshev, I. Brener, Y. S. Kivshar, *Nano Lett.* **2015**, *15*, 5369.
[124] J. Lin, P. Genevet, M. A. Kats, N. Antoniou, F. Capasso, *Nano Lett.* **2013**, *13*, 4269.
[125] X. Yi, X. Ling, Z. Zhang, Y. Li, X. Zhou, Y. Liu, S. Chen, H. Luo, S. Wen, *Opt. Express* **2014**, *22*, 17207.
[126] P. Moitra, B. A. Slovick, W. li, I. I. Kravchencko, D. P. Briggs, S. Krishnamurthy, J. Valentine, *ACS Photonics* **2015**, *2*, 692.
[127] R. Paniagua-Domínguez, Y. F. Yu, A. E. Miroshnichenko, L. A. Krivitsky, Y. H. Fu, V. Valuckas, L. Gonzaga, Y. T. Toh, A. Y. S. Kay, B. Luk'yanchuk, A. I. Kuznetsov, *Nat. Commun.* **2016**, *7*, 10362.
[128] Y. Yang, I. I. Kravchenko, D. P. Briggs, J. Valentine, *Nat. Commun.* **2014**, *5*, 5753.
[129] D. Smirnova, Y. S. Kivshar, *Optica* **2016**, *3*, 1241.
[130] M. R. Shcherbakov, D. N. Neshev, B. Hopkins, A. S. Shorokhov, I. Staude, E. V. Melik-Gaykazyan, M. Decker, A. A. Ezhov, A. E. Miroshnichenko, I. Brener, A. A. Fedyanin, Y. S. Kivshar, *Nano Lett.* **2014**, *14*, 6488.
[131] G. Grinblat, Y. Li, M. P. Nielsen, R. F. Oulton, S. A. Maier, *Nano Lett.* **2016**, *16*, 4635.
[132] Y. Yang, W. Wang, A. Boulesbaa, I. I. Kravchenko, D. P. Briggs, A. Puretzky, D. Geohegan, J. Valentine, *Nano Lett.* **2015**, *15*, 7388.
[133] W. Ye, F. Zeuner, X. Li, B. Reineke, S. He, C.-W. Qiu, J. Liu, Y. Wang, S. Zhang, T. Zentgraf, *Nat. Commun.* **2016**, *7*, 11930.
[134] J. Lee, M. Tymchenko, C. Argyropoulos, P.-Y. Chen, F. Lu, F. Demmerle, G. Boehm, M.-C. Amann, A. Alu, M. A. Belkin, *Nature* **2014**, *511*, 65.
[135] L. Alloatti, C. Kieninger, A. Froelich, M. Lauermann, T. Frenzel, K. Köhnle, W. Freude, J. Leuthold, M. Wegener, C. Koos, *Appl. Phys. Lett.* **2015**, *107*, 121903.
[136] S. Clemmen, A. Hermans, E. Solano, J. Dendooven, K. Koskinen, M. Kauranen, E. Brainis, C. Detavernier, R. Baets, *Opt. Lett.* **2015**, *40*, 5371.
[137] H.-H. Hsiao, A. Abass, J. Fischer, R. Alaee, A. Wickberg, M. Wegener, C. Rockstuhl, *Opt. Express* **2016**, *24*, 9651.
[138] O. Wolf, S. Campione, A. Benz, A. P. Ravikumar, S. Liu, T. S. Luk, E. A. Kadlec, E. A. Shaner, J. F. Klem, M. B. Sinclair, I. Brener, *Nat. Commun.* **2015**, *6*, 7667.
[139] N. Segal, S. Keren-Zur, N. Hendler, T. Ellenbogen, *Nat. Photonics* **2015**, *9*, 180.
[140] E. Almeida, G. Shalem, Y. Prior, *Nat. Commun.* **2016**, *7*, 10367.
[141] M. R. Shcherbakov, P. P. Vabishchevich, A. S. Shorokhov, K. E. Chong, D.-Y. Choi, I. Staude, A. E. Miroshnichenko, D. N. Neshev, A. A. Fedyanin, Y. S. Kivshar, *Nano Lett.* **2015**, *15*, 6985.
[142] J. S. T. Smalley, F. Vallini, S. A. Montoya, L. Ferrari, S. Shahin, C. T. Riley, B. Kante, E. E. Fullerton, Z. Liu, Y. Fainman, *Nat. Commun.* **2017**, *8*, 13793.
[143] T. Galfsky, H. N. S. Krishnamoorthy, W. Newman, E. E. Narimanov, Z. Jacob, V. M. Menon, *Optica* **2015**, *2*, 62.
[144] J. S. Gomez-Diaz, M. Tymchenko, A. Alu, *Opt. Mater. Express* **2015**, *5*, 2313.
[145] A. A. High, R. C. Devlin, A. Dibos, M. Polking, D. S. Wild, J. Perczel, N. P. de Leon, M. D. Lukin, H. Park, *Nature* **2015**, *522*, 192.
[146] D. Keene, M. Durach, *Opt. Express* **2015**, *23*, 18577.
[147] I. Trushkov, I. Iorsh, *Phys. Rev. B* **2015**, *92*.
[148] O. Y. Yermakov, A. I. Ovcharenko, M. Song, A. A. Bogdanov, I. V. Iorsh, Y. S. Kivshar, *Phys. Rev. B* **2015**, *91*, 235423.
[149] H. Dotan, O. Kfir, E. Sharlin, O. Blank, M. Gross, I. Dumchin, G. Ankonina, A. Rothschild, *Nat. Mater.* **2013**, *12*, 158.
[150] M. A. Kats, R. Blanchard, P. Genevet, F. Capasso, *Nat. Mater.* **2013**, *12*, 20.
[151] M. A. Kats, D. Sharma, J. Lin, P. Genevet, R. Blanchard, Z. Yang, M. M. Qazilbash, D. N. Basov, S. Ramanathan, F. Capasso, *Appl. Phys. Lett.* **2012**, *101*, 221101.
[152] P. Hosseini, C. D. Wright, H. Bhaskaran, *Nature* **2014**, *511*, 206.
[153] K. T. Lee, J. Y. Lee, S. Y. Seo, L. J. Guo, *Light-Sci. Appl.* **2014**, *3*, e215.
[154] M. M. Qazilbash, M. Brehm, B. G. Chae, P. C. Ho, G. O. Andreev, B. J. Kim, S. J. Yun, A. V. Balatsky, M. B. Maple, F. Keilmann, H. T. Kim, D. N. Basov, *Science* **2007**, *318*, 1750.
[155] W. Streyer, S. Law, G. Rooney, T. Jacobs, D. Wasserman, *Opt. Express* **2013**, *21*, 9113.
[156] M. Lawrence, N. Xu, X. Zhang, L. Cong, J. Han, W. Zhang, S. Zhang, *Phys. Rev. Lett.* **2014**, *113*, 093901.
[157] F. Monticone, C. A. Valagiannopoulos, A. Alù, *Phys. Rev. X* **2016**, *6*, 041018.
[158] P.-Y. Chen, J. Jung, *Phys. Rev. Appl.* **2016**, *5*, 064018.
[159] R. Fleury, D. L. Sounas, A. Alù, *Phys. Rev. Lett.* **2014**, *113*, 023903.
[160] J. M. Chen, Y. H. Sun, L. B. Zhong, W. J. Shao, J. Huang, F. Liang, Z. Q. Cui, Z. Q. Liang, L. Jiang, L. F. Chi, *Small* **2016**, *12*, 5818.
[161] R. Garcia, A. W. Knoll, E. Riedo, *Nat. Nanotechnol.* **2014**, *9*, 577.
[162] K. Salaita, Y. H. Wang, C. A. Mirkin, *Nat. Nanotechnol.* **2007**, *2*, 145.
[163] C. M. Chang, C. H. Chu, M. L. Tseng, Y. W. Huang, H. W. Huang, B. H. Chen, D. W. Huang, D. P. Tsai, *Plasmonics* **2012**, *7*, 563.
[164] C. H. Chu, M. L. Tseng, C. Da Shiue, S. W. Chen, H. P. Chiang, M. Mansuripur, D. P. Tsai, *Opt. Express* **2011**, *19*, 12652.
[165] M. L. Tseng, Y. W. Huang, M. K. Hsiao, H. W. Huang, H. M. Chen, Y. L. Chen, C. H. Chu, N. N. Chu, Y. J. He, C. M. Chang, W. C. Lin,

D. W. Huang, H. P. Chiang, R. S. Liu, G. Sun, D. P. Tsai, *ACS Nano* **2012**, *6*, 5190.
[166] W. T. Chen, M. L. Tseng, C. Y. Liao, P. C. Wu, S. L. Sun, Y. W. Huang, C. M. Chang, C. H. Lu, L. Zhou, D. W. Huang, A. Q. Liu, D. P. Tsai, *Opt. Express* **2013**, *21*, 618.
[167] M. L. Tseng, B. H. Chen, C. H. Chu, C. M. Chang, W. C. Lin, N. N. Chu, M. Mansuripur, A. Q. Liu, D. P. Tsai, *Opt. Express* **2011**, *19*, 16975.
[168] M. L. Tseng, P. C. Wu, S. L. Sun, C. M. Chang, W. T. Chen, C. H. Chu, P. L. Chen, L. Zhou, D. W. Huang, T. J. Yen, D. P. Tsai, *Laser Photonics Rev.* **2012**, *6*, 702.
[169] B. Lochel, A. Maciossek, H. J. Quenzer, B. Wagner, G. Engelmann, *Sens. Actuators, A* **1995**, *46*, 98.
[170] J. B. Yoon, B. I. Kim, Y. S. Choi, E. Yoon, *IEEE Trans. Microwave Theory Techn.* **2003**, *51*, 279.
[171] W. Haske, V. W. Chen, J. M. Hales, W. T. Dong, S. Barlow, S. R. Marder, J. W. Perry, *Opt. Express* **2007**, *15*, 3426.
[172] C. N. LaFratta, J. T. Fourkas, T. Baldacchini, R. A. Farrer, *Angew. Chem., Int. Ed.* **2007**, *46*, 6238.
[173] S. Maruo, J. T. Fourkas, *Laser Photonics Rev.* **2008**, *2*, 100.
[174] S. Aksu, A. A. Yanik, R. Adato, A. Artar, M. Huang, H. Altug, *Nano Lett.* **2010**, *10*, 2511.
[175] H. W. Gao, J. Henzie, T. W. Odom, *Nano Lett.* **2006**, *6*, 2104.
[176] H. Tao, J. J. Amsden, A. C. Strikwerda, K. B. Fan, D. L. Kaplan, X. Zhang, R. D. Averitt, F. G. Omenetto, *Adv. Mater.* **2010**, *22*, 3527.
[177] M. L. Zhang, N. Large, A. L. Koh, Y. Cao, A. Manjavacas, R. Sinclair, P. Nordlander, S. X. Wang, *ACS Nano* **2015**, *9*, 9331.
[178] C. H. Chu, M. L. Tseng, J. Chen, P. C. Wu, Y.-H. Chen, H.-C. Wang, T.-Y. Chen, W. T. Hsieh, H. J. Wu, G. Sun, D. P. Tsai, *Laser Photonics Rev.* **2016**, *10*, 986
[179] D. Yoo, T. W. Johnson, S. Cherukulappurath, D. J. Norris, S. H. Oh, *ACS Nano* **2015**, *9*, 10647.
[180] P. P. Iyer, M. Pendharkar, J. A. Schuller, *Adv. Opt. Mater.* **2016**, *4*, 1582.
[181] J. Lee, S. Jung, P.-Y. Chen, F. Lu, F. Demmerle, G. Boehm, M.-C. Amann, A. Alu, M. A. Belkin, *Adv. Opt. Mater.* **2014**, *2*, 1057.
[182] M. D. Goldflam, T. Driscoll, D. Barnas, O. Khatib, M. Royal, N. M. Jokerst, D. R. Smith, B.-J. Kim, G. Seo, H.-T. Kim, D. N. Basov, *Appl. Phys. Lett.* **2013**, *102*, 224103.
[183] M. D. Goldflam, M. K. Liu, B. C. Chapler, H. T. Stinson, A. J. Sternbach, A. S. McLeod, J. D. Zhang, K. Geng, M. Royal, B.-J. Kim, R. D. Averitt, N. M. Jokerst, D. R. Smith, H. T. Kim, D. N. Basov, *Appl. Phys. Lett.* **2014**, *105*, 041117.
[184] N. Zhang, Z. Y. Dong, D. X. Ji, H. M. Song, X. Zeng, Z. J. Liu, S. H. Jiang, Y. Xu, A. Bernussi, W. Li, Q. Q. Gan, *Appl. Phys. Lett.* **2016**, *108*, 091105.
[185] X. Su, C. Ouyang, N. Xu, S. Tan, J. Gu, Z. Tian, J. Han, F. Yan, W. Zhang, *IEEE Photonics J.* **2015**, *7*, 5900108.
[186] Y.-W. Huang, H. W. H. Lee, R. Sokhoyan, R. A. Pala, K. Thyagarajan, S. Han, D. P. Tsai, H. A. Atwater, *Nano Lett.* **2016**, *16*, 5319.
[187] J. Chou, L. Parameswaran, B. Kimball, M. Rothschild, *Opt. Express* **2016**, *24*, 24265.
[188] M. Decker, C. Kremers, A. Minovich, I. Staude, A. E. Miroshnichenko, D. Chigrin, D. N. Neshev, C. Jagadish, Y. S. Kivshar, *Opt. Express* **2013**, *21*, 8879.
[189] J. W. He, Z. W. Xie, W. F. Sun, X. K. Wang, Y. D. Ji, S. Wang, Y. Lin, Y. Zhang, *Plasmonics* **2016**, *11*, 1285.